Astronomy & Astrophysics manuscript no. IIn-sample-paper
June 14, 2019

arXiv:1906.05812v1 [astro-ph.SR] 13 Jun 2019

Type IIn supernova light-curve properties measured from an untargeted survey sample[*]

A. Nyholm[1], J. Sollerman[1], L. Tartaglia[1], F. Taddia[1], C. Fremling[2], N. Blagorodnova[3], A. V. Filippenko[4,5], A. Gal-Yam[6], D. A. Howell[7,8], E. Karamehmetoglu[1], S. R. Kulkarni[2], R. Laher[9], G. Leloudas[10], F. Masci[9], M. M. Kasliwal[2], K. Morå[11], T. J. Moriya[12], E. O. Ofek[13], S. Papadogiannakis[11], R. Quimby[14], U. Rebbapragada[15], and S. Schulze[6]

[1] Department of Astronomy and the Oskar Klein Centre, Stockholm University, AlbaNova, 10691 Stockholm, Sweden (e-mail: `anders.nyholm@astro.su.se`)
[2] Division of Physics, Mathematics, and Astronomy, California Institute of Technology, Pasadena, CA 91125, USA
[3] Department of Astrophysics/IMAPP, Radboud University, Houtlaan 4, 6525 XZ Nijmegen, The Netherlands
[4] Department of Astronomy, University of California, Berkeley, CA 94720-3411, USA
[5] Miller Senior Fellow, Miller Institute for Basic Research in Science, University of California, Berkeley, CA 94720, USA
[6] Department of Particle Physics and Astrophysics, Weizmann Institute of Science, 234 Herzl St., Rehovot, 76100, Israel
[7] Las Cumbres Observatory, 6740 Cortona Drive, Suite 102, Goleta, CA 93117-5575, USA
[8] Department of Physics, University of California, Santa Barbara, CA 93106-9530, USA
[9] Infrared Processing and Analysis Center, California Institute of Technology, 1200 E. California Blvd, Pasadena, CA 91125, USA
[10] DTU Space, National Space Institute, Technical University of Denmark, Elektrovej 327, 2800 Kgs. Lyngby, Denmark
[11] Department of Physics and the Oskar Klein Centre, Stockholm University, AlbaNova, 10691 Stockholm, Sweden
[12] National Astronomical Observatory of Japan, 2-21-1 Osawa, Mitaka, Tokyo 181-8588, Japan
[13] Benoziyo Center for Astrophysics, Weizmann Institute of Science, 76100 Rehovot, Israel
[14] Department of Astronomy/Mount Laguna Observatory, San Diego State University, 5500 Campanile Drive, San Diego, CA 92812-1221, USA
[15] Jet Propulsion Laboratory, California Institute of Technology, Pasadena, CA 91109, USA

Received; accepted

Abstract

The evolution of a Type IIn supernova (SN IIn) is governed by the interaction between the SN ejecta and a hydrogen-rich circumstellar medium (CSM). SNe IIn thus allow us to probe the late-time mass-loss history of their progenitor stars. We present a sample of SNe IIn from the untargeted, magnitude-limited surveys of the Palomar Transient Factory (PTF) and its successor, the intermediate PTF (iPTF). To date, statistics on SN IIn optical light curve properties have generally been based on small ($\lesssim 10$ SNe) samples from targeted SN surveys. SNe IIn found and followed by the PTF/iPTF were used to select a sample of 42 events with useful constraints on the rise times as well as with available post-peak photometry. The SNe were discovered in 2009–2016 and have at least one low-resolution classification spectrum, as well as photometry from the P48 and P60 telescopes at Palomar Observatory. We study the light-curve properties of these SNe IIn using spline fits (for the peak and the declining portion) and template matching (for the rising portion). We study the peak-magnitude distribution, rise times, decline rates, colour evolution, host galaxies, and K-corrections of the SNe in our sample. We find that the typical rise times are divided into fast and slow risers as 20 ± 8 d and 50 ± 15 d, respectively. The decline rates could possibly be divided into two groups (with slopes $0.013 \pm 0.008\,\mathrm{mag\,d^{-1}}$ and $0.040 \pm 0.014\,\mathrm{mag\,d^{-1}}$), but this division has weak statistical significance. We find no significant correlation between the peak luminosity of SNe IIn and their rise times, but the more luminous SNe IIn are generally found to be more durable and the slowly rising SNe IIn are generally found to be slowly declining. The SNe in our sample were hosted by galaxies of absolute magnitude $-22 \lesssim M_g \lesssim -13$ mag. The K-corrections at light-curve peak of the SNe in our sample are found to be within 0.2 mag for the observer's frame r-band, for SNe IIn at redshifts $z < 0.25$. Applying K-corrections and including also ostensibly "superluminous" SNe IIn, we find that the peak magnitudes are $M^r_{\mathrm{peak}} = -19.18 \pm 1.32$ mag. We conclude that the occurrence of conspicuous light-curve bumps in SNe IIn, such as in iPTF13z, is limited to $1.4^{+14.6}_{-1.0}$ % of the SNe IIn. We also investigate a possible subtype of SNe IIn with a fast rise to a $\gtrsim 50$ d plateau followed by a slow, linear decline.

Key words. supernovae : general – supernovae: individual: PTF09tm, PTF09uy, PTF09bcl, PTF10cwl, PTF10cwx, PTF10ewc, PTF10fjh, PTF10flx, PTF10gvd, PTF10gvf, PTF10oug, PTF10qwu, PTF10tel, PTF10tyd, PTF10vag, PTF10weh, PTF10xgo, PTF10abui, PTF10achk, PTF10acsq, PTF11fzz, PTF11mpg, PTF11oxu, PTF11qnf, PTF11qqj, PTF11rfr, PTF11rlv, PTF12cxj, PTF12frn, PTF12glz, PTF12ksy, iPTF13agz, iPTF13aki, iPTF13asr, iPTF13cuf, iPTF14bcw, iPTF14bpa, iPTF15aym, iPTF15bky, iPTF15blp, iPTF15eqr, iPTF16fb.

1. Introduction

A supernova (SN) having a spectrum showing Balmer emission lines with narrow or intermediate-width central components

---

[*] Based in part on observations made with the Palomar Transient Factory and intermediate Palomar Transient Factory surveys.

and broad line wings is classified as a Type IIn SN. This SN classification (where "II" indicates presence of hydrogen and "n" stands for narrow) was proposed by Schlegel (1990) and reached wider use via (for example) the review by Filippenko (1997). It has been shown via observations and modelling (e.g., Chevalier & Fransson 1994; Smith 2016; Dessart et al. 2016) that the SN IIn spectral signature arises from the interaction of SN ejecta with a hydrogen-rich circumstellar medium (CSM), where the shocks formed when the ejecta sweep up the CSM convert the kinetic energy of the ejecta into radiated energy.

A SN IIn spectrum is produced in a process involving the SN environment, and shows little direct signatures of the explosion itself. Many different scenarios can therefore potentially give rise to SN IIn spectral signatures, making it difficult to tell whether a core-collapse (CC) SN explosion or a violent but nondisruptive stellar outburst sent the ejecta off (e.g., Dessart et al. 2009). Whereas the ejecta-CSM interaction makes SNe IIn useful probes of progenitor mass-loss histories, SNe IIn are also challenging to understand since the nature of the underlying energy source remains elusive.

The spectroscopic criteria defining the SN IIn classification makes them spectroscopically somewhat similar, but their peak absolute magnitudes vary greatly, as do their light-curve shapes and the presence of undulations and bumps in their light curves. The wide range of light-curve properties shown by SNe IIn indicates significant variety in both CSM and ejecta properties (e.g., Moriya et al. 2014), suggesting that different mechanisms and progenitor channels lead to the SNe IIn we observe (Smith 2014).

SNe IIn are intrinsically rare. A volume-limited SN sample from the targeted Lick Observatory Supernova Search (LOSS; Li et al. 2011) showed that $\sim 7\%$ of all CC SNe are SNe IIn. Their diverse properties call for large samples in order to improve our understanding of this SN type. However, the current SN IIn literature is skewed toward a small number of well-studied events, often being nearby (at redshifts $z \lesssim 0.02$) or characterised by some unusual property. Our aim in this paper is to study a sample of SNe IIn from the untargeted Palomar Transient Factory (PTF; Law et al. 2009) survey and its successor, the intermediate PTF (iPTF; Kulkarni 2013), with emphasis on the SN IIn optical light curves.

Among the SN IIn samples presented in the literature are works concerning SN data release and analysis (e.g., Kiewe et al. 2012; Taddia et al. 2013, 2015), but also environmental (e.g., Kelly & Kirshner 2012; Habergham et al. 2014; Taddia et al. 2015; Galbany et al. 2018) and SN rate studies (Li et al. 2002, 2011), as well as precursor outburst analysis (e.g., Ofek et al. 2014c; Bilinski et al. 2015). In Table 1 we present a summary of the SN IIn samples in the literature concerning optical light-curve properties. The peak absolute magnitudes of the SNe IIn studied by Kiewe et al. (2012) and Taddia et al. (2013) were in the interval $-19 \lesssim M_B \lesssim -17$ mag, consistent with the findings of Li et al. (2011) as well as Richardson et al. (2002, 2014), two studies that include luminosity functions of SNe IIn.

The decline behaviour after maximum brightness differs considerably among SNe IIn. Among slowly declining SNe IIn, SN 1988Z has become a benchmark object in the literature (Stritzinger et al. 2012; Habergham et al. 2014; Turatto et al. 1993). Other SNe IIn decline considerably faster, with SN 1998S (Liu et al. 2000; Fassia et al. 2000) commonly given as a specimen. Apart from decline rates, light-curve shapes can also distinguish SNe IIn. SN 1994W (Sollerman et al. 1998) often exemplifies SNe IIn with plateaus in their light curves followed by a sharp decline in brightness, sometimes called SNe IIn-P (Mauerhan et al. 2013a). Some SNe IIn exhibit distinct episodes of rebrightening ("bumps"), breaking their decline in brightness (e.g., Stritzinger et al. 2012; Graham et al. 2014; Martin et al. 2015; Nyholm et al. 2017).

An important finding facilitated by modern surveys like the PTF is that some SNe IIn have precursor outbursts in the years before the main SN outburst. Sample studies (Ofek et al. 2014c; Bilinski et al. 2015) give inconclusive results regarding whether precursor events are common (possibly owing to the different methods used in the respective studies). Precursor outbursts suggest connections between SNe IIn and such phenomena as luminous blue variable (LBV; Humphreys & Davidson 1994) outbursts (Smith et al. 2011) as well as other SN impostors (Van Dyk et al. 2000; Van Dyk & Matheson 2012).

The SN IIn samples in the literature have uneven photometric coverage of the SNe during the rising phase of their light curves. A number of the benchmark SN IIn events (e.g., SN 1988Z, Stathakis & Sadler 1991; SN 1995N, Fransson et al. 2002; SN 2005ip and SN 2006jd, Stritzinger et al. 2012) lack well-determined rise times to peak. The literature sample of light curves shown by Taddia et al. (2015, their figure 10) also indicates the lack of pre-peak photometry for a number of otherwise well-characterised SNe IIn. The existence of a correlation between rise time and peak magnitude for SNe IIn has been investigated (Ofek et al. 2014a,b; Moriya & Maeda 2014) and suggested to exist (Ofek et al. 2014b). To further study this possible correlation, more knowledge of SNe IIn rise times is needed.

By using a sample from the high-cadence and untargeted PTF/iPTF search to study light-curve rise times, maximum absolute magnitudes, and light-curve slopes during the decline phase, we can characterise the SN IIn class. The untargeted nature of the PTF/iPTF survey provides a sample which is not biased toward SNe in luminous, metal-rich, high-star-formation-rate host galaxies. The high cadence of PTF/iPTF also allows us to put tighter constraints on the rise times of our SNe.

In Sect. 2, we present the SN search and follow-up observations done by the PTF/iPTF and the telescopes and instruments used, as well as the reduction methods adopted to prepare the photometric data for analysis. We discuss the selection of our SN IIn sample as well as its properties in Sect. 3, including a discussion of distances and foreground extinction of the SNe. In Sect. 4, we measure the light-curve peak magnitudes and peak epochs (Sect. 4.1) and the decline rates of the SNe (Sect. 4.2). We also study the light-curve rise times (Sect. 4.3), as well as possible correlations between these light-curve-shape parameters (Sect. 4.4). Colour curves are examined using our optical photometry (Sect. 4.5). A simple study of the host galaxies of our sample SNe is done, using Sloan Digital Sky Survey (SDSS) and Panoramic Survey Telescope and Rapid Response System (Pan-STARRS) photometry for the hosts (Sect. 4.7). In Sect. 5, we discuss our results and highlight some sample SNe with interesting properties, and estimate the fraction of SNe IIn having light curve bumps. We summarise our conclusions in Sect. 6. In Appendix A, we use the spectra of our SNe to study their K-corrections.

2. Observations and data reduction

The PTF and iPTF surveys did untargeted searches for astronomical transients during 2009–2017, using the 1.2-m Samuel Oschin telescope (known as P48) at Palomar Observatory. P48 equipped with the CFH12K mosaic CCD gave a 7.26 $\deg^2$

field of view (Law et al. 2009). Images were taken through either a Mould R-band filter (Law et al. 2009; Ofek et al. 2012; Laher et al. 2014) or an SDSS g-band filter (Fukugita et al. 1996), giving a limiting magnitude of $R \approx 20.5$ or $g \approx 21$ (respectively) under typical conditions. After image processing and an automatic initial selection of candidates (Cao et al. 2016), a human scanner vetted the images and flagged interesting candidates for follow-up photometry and spectroscopy on other telescopes. All SNe in the sample presented in this paper were found independently with the P48. Whereas several different pipelines were used for photometry in P48 images during the course of PTF/iPTF, all SN photometry from P48 presented in this paper has been extracted with the PTFIDE (PTF Image Differencing and Extraction; Masci et al. 2017) pipeline.

An important instrument for photometric follow-up observations during PTF/iPTF was the 1.52-m telescope (known as P60) at Palomar Observatory. The telescope was used for imaging with the GRBCam camera (Cenko et al. 2006) or the Spectral Energy Distribution Machine (SEDM) integral field spectrograph (Blagorodnova et al. 2018) using SDSS gri filters. A typical strategy with the P60 was to obtain SDSS gri images of a SN field with a cadence of 1 d or 3 d (for young SNe) and a cadence of 6 d for older SNe. Other cadences and filters (e.g., SDSS z and Johnson B) were also sometimes used. For this paper, SN photometry of the images from P60 (both GRBCam and SEDM) was done with the FPipe pipeline (Fremling et al. 2016).

All magnitudes reported here for SNe in our sample are AB magnitudes from PSF photometry on host-subtracted images.

Classification spectra of identified transients were obtained continuously by members of the PTF/iPTF collaboration, using different telescopes with apertures ranging from 2 to 10 m, and their spectrographs. While some SNe were monitored extensively with spectroscopy, the majority of the SNe in our sample only have ~ 1 spectrum. The classification spectra used in this work are shown in Fig. 1 and are listed in Table 2.

3. The sample

A total of 3018 confirmed SNe was found by PTF/iPTF in the years 2009–2017, all spectroscopically classified by the collaboration using template-matching software like SNID (Blondin & Tonry 2007), Gelato (Harutyunyan et al. 2008), or Superfit (Howell et al. 2005). Classifications of the PTF/iPTF SNe were done by a joint effort of members of the PTF/iPTF collaboration, involving discussions of ambiguous cases.

Among the SNe found and spectroscopically classified by PTF/iPTF during 2009–2017, a total of 111 are SNe IIn. These SNe IIn are located at declinations $-23^\circ < \delta < +75^\circ$ and in the redshift interval $0.0071 < z < 0.31$. The mean z of the total SN IIn sample is 0.083 and the median z is 0.07. For our SN IIn sample, we made a selection based on criteria related to the availability of photometry for the rising and declining portions of the SN light curves. Selection of our final sample of SNe IIn was conducted according to the following steps.

To obtain photometry of even quality from the P48 images, the PTFIDE pipeline was run on all available R and g images from P48 for the locations of the 111 SNe in the initial sample, to get forced template-subtracted photometry (using the procedure from Masci et al. 2015).

For the light curves thus obtained, we applied the constraint that a photometric upper limit must occur less than 40 d before the epoch of the PTF/iPTF discovery of the SN in order to allow a useful constraint on the rise time. This decreased the sample from 111 to 55 events. Including also inspection of the preliminary reductions of the P60 photometry, only SNe IIn with detections past 40 d after discovery were kept in the sample. After final refinement using the fully reduced P60 photometry, we were left with a sample of 42 SNe IIn with satisfactory light-curve coverage. The time intervals considered in the selection were in the observer's frame.

Our SN sample selection process is summarised in Table 3. The classification spectra in the region around Hα for these 42 SNe IIn are provided in Fig. 1. Basic properties of the SNe in the sample are summarised in Table 4. In the cases when the PTF/iPTF discovery of a SN constituted an independent discovery of a SN already found (or later found) by others, a reference is given in Table 4. The 42 light curves are shown in Fig. 2. The SNe in the sample are covered in $BgrRiz$ photometry (but not all SNe are covered in all photometric bands).

The photometry presented here for the 42 SNe will be made available via the VizieR[1] database (Ochsenbein et al. 2000) and the classification spectra and the photometry made available via WISeREP[2] (Yaron & Gal-Yam 2012).

Table 4 shows that most of the SNe IIn in our sample have been mentioned in the literature, mostly by three sample studies (Ackermann et al. 2015; Ofek et al. 2014b,c) as well as Circulars and other nonrefereed sources. These sample studies mainly concerned themselves with R-band photometry (Ofek et al. 2014b,c) or searches for γ-ray emission from the positions of the SNe (Ackermann et al. 2015), and did not publish full light curves. PTF10tel (= SN 2010mc) and its precursor activity is the topic of a paper by Ofek et al. (2013) and PTF12glz was studied by Soumagnac et al. (2019). Early-time spectra of PTF10gvf and PTF10tel were studied in the spectral sample paper by Khazov et al. (2016). For consistency, we will refer to the SNe by their PTF/iPTF names, even in the cases when IAU (International Astronomical Union) designations exist.

The superluminous SNe (SLSNe) IIn deserve special attention. A $M < -21$ mag limit has commonly been used to define SLSNe (Gal-Yam 2012, 2018) but it is not clear whether SNe IIn fulfilling this criterion constitute a separate population of events (e.g. Moriya et al. 2018; Gal-Yam 2018). During the time when the SNe IIn in our sample were found and classified, the $M < -21$ mag limit was in common use and the 111 SNe Type IIn that we used to construct our final sample are therefore typically fainter at peak than this limit.

Not all SLSNe Type II display narrow Balmer lines in their spectra (Inserra et al. 2018). In the full PTF/iPTF catalogue of spectroscopically classified SNe a total of 15 SLSNe II are listed. For 7 of the SNe, the spectra are either noisy or contaminated by host galaxy emission lines as to make a SLSN Type IIn classification difficult. The spectrum of PTF12gwu has weak Balmer lines (Perley et al. 2016), but possibly broad. The remaining 7 of the SLSN Type II display a narrow Hα emission component ostensibly making them SLSNe Type IIn. Applying our criteria (see above) requiring a maximum gap of 40 d between discovery epoch and last pre-discovery upper limit, leave 6 SLSNe Type IIn. Also requiring photometry past 40 days after discovery leaves 5 SLSNe IIn: PTF10heh, PTF12mkp, PTF12mue, iPTF13duv and iPTF13dol. The PTF/iPTF photometry shows that these 5 SLSNe Type IIn had light-curve peaks at ~ -21 mag. The photometry for two of these (PTF12mue and iPTF13duv) is too sparse to allow us to further characterise their light curves.

---

[1] `http://vizier.u-strasbg.fr`

[2] `https://wiserep.weizmann.ac.il`

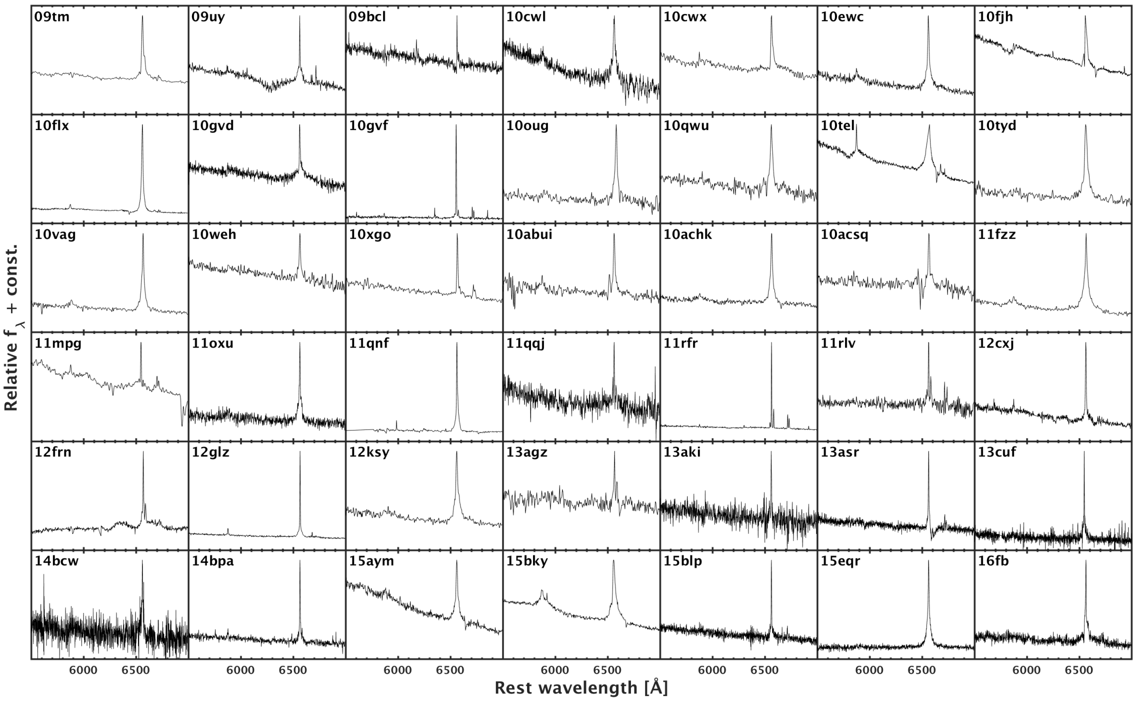

Figure 1 The classification spectra of the 42 SNe IIn included in our study, each showing the Hα narrow or intermediate-width emission characteristic of SNe IIn. Details of the spectra are given in Table 2. In some spectra, telluric B-band absorption (or residual, incompletely removed absorption) is visible at 6860 Å in the observed frame of reference. Spectra of PTF10weh and PTF12cxj were presented by Ofek et al. (2014c), spectra of PTF10gvf by Khazov et al. (2016) and of PTF10tel by Ofek et al. (2013); Khazov et al. (2016).

We will therefore use the sample of 111 PTF/iPTF SNe IIn "as is" with respect to the $M < -21$ mag SLSN criterion when selecting our SN IIn sample. For discussing whether the SLSNe Type IIn constitute a separate population of SNe, we will include the additional 3 SLSNe IIn (PTF10heh, PTF12mkp and iPTF13dol) in the peak-magnitude distribution and in our luminosity function study in Sect. 4.6. For comparison purposes, we will also include PTF10heh and PTF12mkp when discussing the duration-luminosity phase space (DLPS) in Sect. 4.8. PTF10heh and PTF12mkp are already presented in the literature (Perley et al. 2016). iPTF13dol was found by iPTF on 2013 September 29 at $\alpha = 22^{\mathrm{h}}22^{\mathrm{m}}07\overset{\mathrm{s}}{.}27$, $\delta = 12°30'39\overset{''}{.}9$ (J2000.0) and $z = 0.225$. A study dedicated to SLSNe II from PTF is ongoing (Leloudas et al., in prep.).

3.1. Distances and extinctions

In this paper, our SN distance estimates are based on the SN redshifts, and we assume a ΛCDM cosmology and use the cosmological parameters $H_0 = 70.0\,\mathrm{km\,s^{-1}\,Mpc^{-1}}$, $\Omega_\Lambda = 0.721$, and $\Omega_M = 0.279$ (Hinshaw et al. 2013). We use a method based on the NASA/IPAC Extragalactic Database (NED) routine (following Mould et al. 2000a,b) to compensate for Virgo, Great Attractor, and Shapley cluster infall in our distance estimates. The redshifts of the sample SNe were measured by fitting Gaussian profiles to the Hα emission lines of their spectra. The histogram of the redshifts is shown in Fig. 3.

Milky Way (MW) extinction values from Schlafly & Finkbeiner (2011) were obtained via NED. Extinctions for different photometric bands were calculated using the `extinction` function by Ofek (2014) based on Cardelli et al. (1989) and assuming an absorption-to-reddening ratio $R_V = 3.1$. If SN spectra showed a clear Na I D absorption doublet, host-galaxy extinction was computed using Taubenberger et al. (2006, their Eq. 1). Such indications of host-galaxy extinction were seen only in the spectra of PTF09tm ($E(B-V) = 0.16$ mag), PTF11qnf (0.72 mag), and PTF12frn (0.57 mag). We remind the reader that given the quality and resolution of our classification spectra, we are not very sensitive to this method. The effects of these assumptions on our results are discussed in Sect. 5.2.

4. Analysis

In the following analysis we characterise the main light-curve parameters, i.e., peak absolute magnitude and its epoch, light-curve decline rates, and rise times. We also investigate possible correlations between these properties. We describe the optical colours and the host-galaxy properties. Finally, we compare our observations to simple models in order to derive information on the CSM and on the SN progenitor scenarios. In our analysis, we apply corrections to the following SNe: for PTF10acsq, a correction (found by interpolation on P60 r-band detections) of 0.07 mag was added to the P48 R-band; by similar interpolation on P60 g-band detections, for iPTF15aym 0.72 mag was added to the P48 g-band, and for iPTF15eqr 0.19 mag was added (by interpolation on P60 r) to the P48 R-band.

4.1. Peak magnitudes and peak times

The differences in cadence, photometric errors, as well as intrinsic light-curve shapes make the use of a single analytical

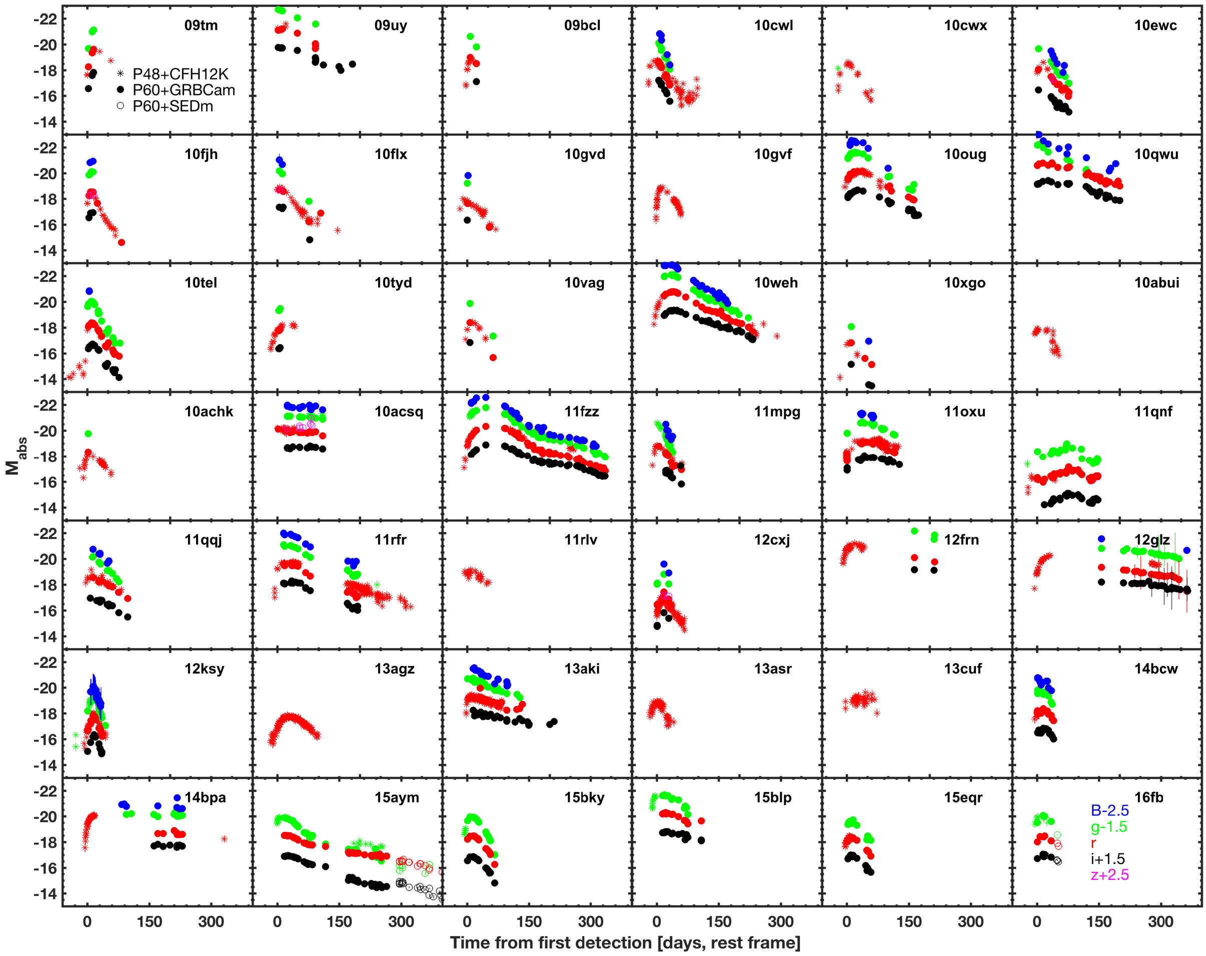

Figure 2 The light curves of the 42 SNe IIn in the sample, with time shown in the rest frame. In these plots, for clarity, we do not show photometric upper limits.

template difficult for characterising the light curves. Instead, we use cubic smoothing splines (CSS; de Boor 2001) to fit the light curves and to find peak-magnitude values and times of peak for our sample SNe. Before fitting, we convert the photometry from AB magnitudes to flux densities (using the `convert_flux` function from Ofek 2014).

The fitting of a CSS to a set of data is determined by the smoothing parameter s, where the fit approaches a least-squares (LSQ) fit of a straight line as $s \to 0$, whereas the fit approaches a cubic-spline interpolant between each data point as $s \to 1$. To objectively choose an s value for each light curve, we proceed in the following way.

For a grid of 45 s values with decadal spacing in the interval $10^{-5} \leq s \leq 0.9$, a CSS fit was made for each s value. For each CSS fit, the number of degrees of freedom (d.o.f.) was computed as the number of observations minus the number of parameters of the CSS fit, and then used to calculate the χ^2 values of each CSS fit (per d.o.f. – i.e., the reduced χ^2 values, $\chi^2_{\mathrm{d.o.f.}}$).

For selecting the s value, we use the Akaike Information Criterion (AIC; see, e.g., Sect. 2 of Davis et al. 2007) as our statistic. The AIC punishes models of high orders (i.e., "over-parametrised" models). As we desire a CSS fit capturing the large-scale behaviour of the light curve (while not being sensitive to smaller fluctuations), we choose to consider values of $s < 0.1$. We generally select the smoothing parameter s giving the smallest AIC value for $s < 0.1$. If no minimum of the AIC value is found for $s < 0.1$, an s value is selected corresponding to the AIC value 3σ above the mean AIC value for the interval $0.01 < s < 0.1$.

Armed with our selected s parameter for each SN, Monte Carlo (MC) experiments were done to estimate the uncertainties of the maximum flux density and the peak epoch. For each MC run, pseudo data points were generated for each epoch in the light curve, drawn from Gaussian distributions around the original data points (from within the 1σ photometric error bars). For the s value found above, CSS fits are made to each such pseudo light curve, and maximum flux density and peak epoch are determined for each of them. The mean values of the highest flux density and its epoch are used as the final values, and their standard deviations are used as their 1σ uncertainties. This process is illustrated in Fig. 4. The CSS fits are shown in Fig. 5, along with the measured peak of each light curve. The peak magnitudes are presented in Table 5, where the absolute magnitudes are corrected for extinction. In our later analysis of decline rates and rise times, the SNe with peak time error > 10 d (marked with red crosses in Fig. 5) are excluded.

To evaluate if one or more populations can be distinguished among the SNe when considering a given property (such as peak absolute magnitude), we use Gaussian mixture models (GMM) following Papadogiannakis et al. (2019). The method works by applying an increasing number of Gaussian distributions to the data, using the AIC for each step to evaluate the significance

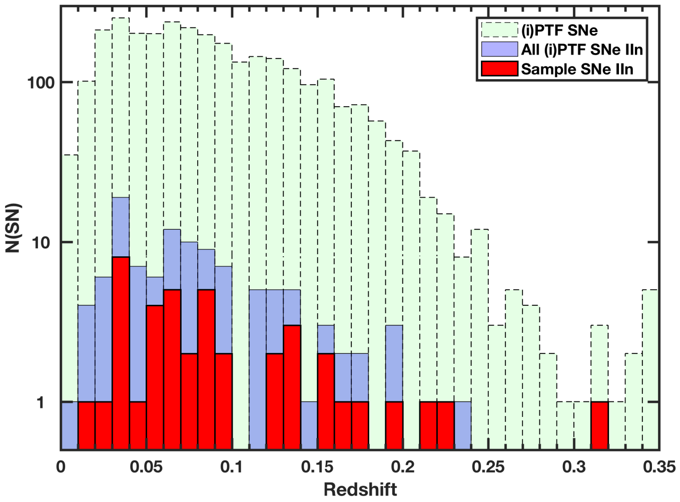

Figure 3 Histogram of the redshifts for the 42 SNe IIn included in our sample. The redshifts of the full PTF/iPTF sample of 111 SNe IIn is shown in blue. For comparison, the redshifts of the full PTF/iPTF yield of spectroscopically classified SNe (for $z < 0.35$) is shown in green.

of each combination of Gaussians. The best combination of Gaussians is the one giving the lowest value of AIC. Given our small sample we also tried the Bayesian information criterion (BIC), which is considered to rule out over-parametrised models in a way stronger than the AIC (Liddle 2004). Following Sollerman et al. (2009) we consider models separated by ΔIC $\geq$ 6 from the surrounding models as significant. Owing to our relatively small sample size (42 SNe), we limit ourselves to examining 1 to 3 combined Gaussians.

Applying GMM to the distribution of peak absolute magnitudes, the AIC would prefer a combination of 3 Gaussians describing the distribution. However, the BIC favours a single Gaussian describing the peak absolute magnitude distribution. For simplicity, we will consider this single Gaussian (Fig. 6) in our analysis.

The observed peak-magnitude distribution for the sample is shown in Fig. 6 along with the best-fit Gaussian distributions. The g-band photometry was used when measuring four of the SNe (see Table 5). Of our sample SNe IIn, the peak magnitudes within 1σ from the mean peak magnitudes range between -17.4 and -20.5 mag (a factor of 17 in luminosity). We see that $\sim 83\%$ of the SNe IIn from our sample lie between -17.4 mag and -20.5 mag, suggesting that the distribution of peak magnitudes is not completely Gaussian.

Comparing these peak-magnitude ranges to known SNe IIn in the literature (central panel in Fig. 6), we notice that many well-studied SNe IIn peak within the -17.4 to -20.5 mag range as found above. In the bottom panel of Fig. 6, we show the 39 SNe with determined peak epoch and mark the -17.4 to -20.5 mag range with horizontal dashed lines. The large total range of peak absolute magnitudes for the sample (~ 5 mag) is clearly illustrated.

4.2. Light-curve decline rates

Among the first events classified as SNe IIn, it was noticed that some faded slowly compared to other CC SNe. SN 1988Z (Stathakis & Sadler 1991; Aretxaga et al. 1999) declined at $\sim 0.2\,\mathrm{mag}\,(100\,\mathrm{d})^{-1}$ in the R-band past 100 d after maximum brightness. SN 1998S (Liu et al. 2000; Fassia et al. 2000) instead had a fast initial decline of $\sim 2.5\,\mathrm{mag}\,(100\,\mathrm{d})^{-1}$ in the R-band. Sample measurements of SN IIn decline rates have been presented by Taddia et al. (2013) and Kiewe et al. (2012).

In the MC experiments with the CSS fits (Sect. 4.1), the flux-density values at 50 (but also 100, 150, 200, and 250) days past peak were measured (if occurring within the time range where the SN was detected) for determination of decline rates in these time intervals. This is done for the photometry obtained in the $BgrRi$ bands, in the cases where the coverage exceed 50 d (rest frame) after the peak times given in Table 5. The decline rates for 0–50 d for the $R/r/g$ bands are provided in Table 5. The distribution of the decline rates between 0 and 50 d post-peak (for the 27 SNe possible to measure) is shown in the top panel of Fig. 7 as a histogram.

A GMM test (Sect. 4.1) gives inconclusive results, with the BIC significantly suggesting one Gaussian distribution. Such a single distribution has $0.012 \pm 0.008\,\mathrm{mag\,d}^{-1}$ and is overplotted in the top panel of Fig. 7. However, AIC suggests two Gaussian distributions, but with weak significance: one of slow decliners ($0.013 \pm 0.008\,\mathrm{mag\,d}^{-1}$) and one of fast decliners ($0.040 \pm 0.014\,\mathrm{mag\,d}^{-1}$). Note that no K-corrections were applied when measuring these rates. Overplotting these decline rates on the actual SN light curves (scaled to match at peak brightness) in the bottom panel of Fig. 7 visualises this result. The middle panel shows that most of our fast-declining SNe IIn are actually declining faster than SN 1998S (considered as a prototypical fast decliner).

To allow a straightforward comparison between decline rates of SNe at different redshifts, in Fig. 8 we plot the decline rates as a function of the effective rest wavelength (for the filter used and the redshift of the SN in question, as in for example González-Gaitán et al. 2015). In the 0–50 d panel, we see the lack of slow decliners in the bluer bands. This is similar to what is seen in other SN types (e.g., SNe IIP; Valenti et al. 2016) where also the bluer bands exhibit the fastest decline rates. For the panels showing times > 50 d, the number of SNe gets smaller. This likely involves observational bias, since these SNe are becoming too faint for us to monitor. SNe IIn like SN 2005ip (Stritzinger et al. 2012) had an initial rapid decline, followed by a durable (> 100 d) fainter plateau. Such faint and late plateaus would be missed in this study for many of our SNe, owing to their large distances.

Although SNe IIn are assumed to primarily be driven by circumstellar interaction (CSI), we can use the decline rates found here to evaluate if radioactive decay can be a possible energy source in some of the SNe in our sample. For CC SNe such as SNe IIP, the rate of decay for $^{56}\mathrm{Co} \rightarrow ^{56}$ Fe determine the light-curve slope around ~ 200 d after light-curve peak. Figure 8 shows that some SNe around 200 d after peak have decline rates consistent with radioactive decay. From Fig. 2, it can be seen that these SNe have absolute magnitudes of $M \approx -17$ mag at this time. Nadyozhin (1994, his Eq. 19) indicates that the original ^{56}Ni mass necessary to drive such a light curve is $\sim 1\,\mathrm{M}_\odot$, which is an order of magnitude more than for normal SNe IIP (e.g., Hamuy 2003; Rubin et al. 2016). Most SNe in our sample indeed decline more slowly than the radioactive decay, and we consider radioactive decay as an unrealistic mechanism to explain the late-time luminosities and decay rates seen in our sample of SNe IIn.

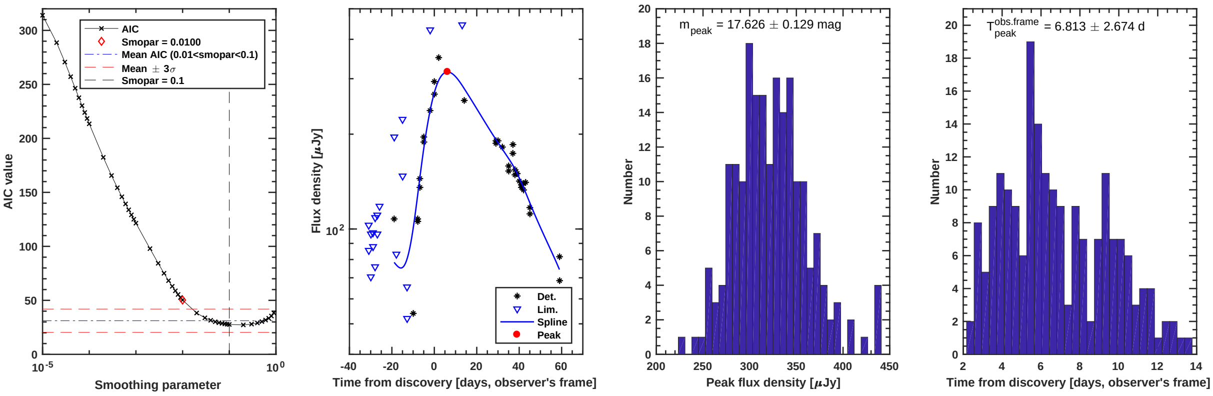

Figure 4 *Left to right:* AIC values as a function of the smoothing parameter of the attempted spline fits, light curve (in flux density),

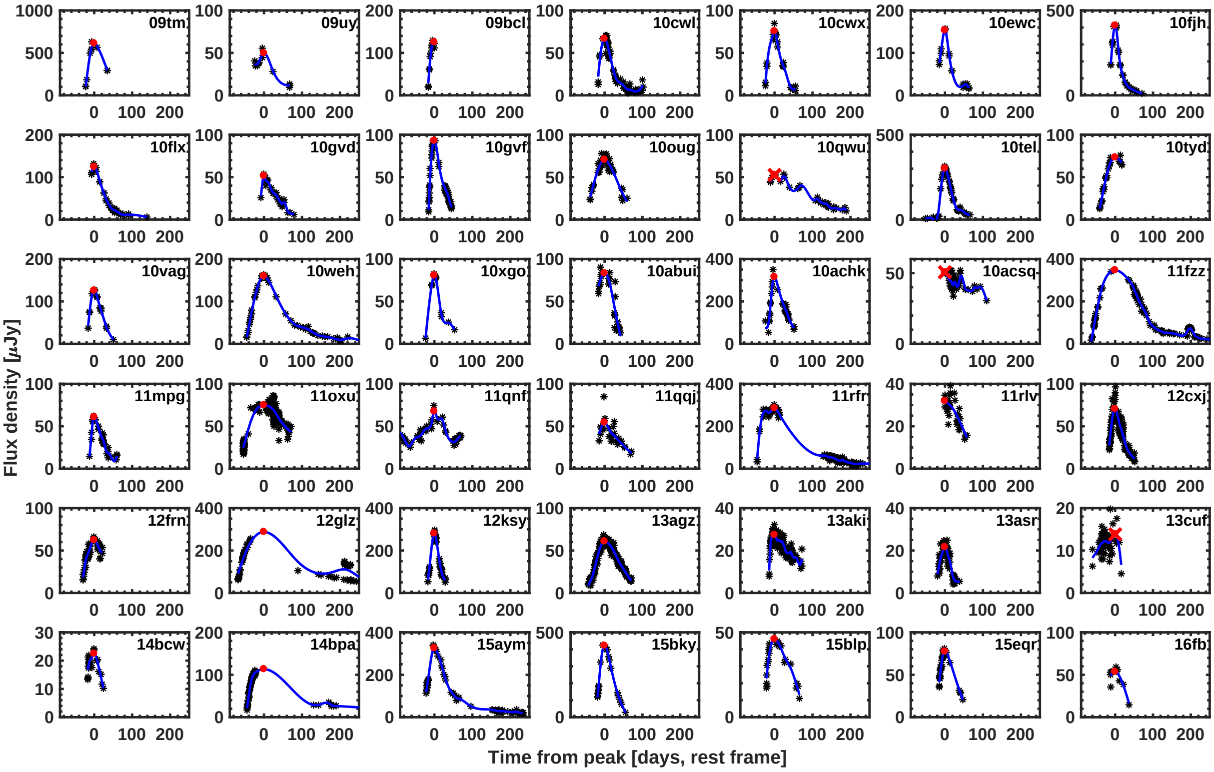

Figure 5 CSS splines fit to our SN IIn light curves, to determine the times and magnitudes of the light-curve peaks (Sect. 4.1). Photometric bands are specified in Table 5. The CSS fit is indicated by a blue curve, and the peak of the light curve is marked by a red dot. The smoothing parameter s for each SN is reported in Table 5. The SNe with peak-time error $>$ 10 d (PTF10qwu, PTF10acsq, iPTF13cuf) are marked with red crosses.

4.3. Light-curve rise times

By fitting a function to the rising portion of a SN light curve, the starting time of the light curve can be constrained, given the assumption that the unseen early portion of the rise is smooth and that the fitted function is consistent with the prediscovery upper limits in the photometry. Functions commonly used for such fits are power-law functions (González-Gaitán et al. 2015; Ofek et al. 2014b; Cowen et al. 2010) or exponential functions (González-Gaitán et al. 2015; Ofek et al. 2014b; Bazin et al. 2009), which may have little physical motivation but allow quantification of the SN light-curve rise.

In our work, we are primarily interested in finding a consistent way to measure the rise times of our sample SNe IIn, without characterising the shape of the light-curve rise in detail for each SN. For this purpose, we use a power-law light-curve template based on a well-studied, nearby SN in our sample.

Based on the procedure in Sect. 4.1, the SNe with peak time error $>$ 10 days (PTF10qwu, PTF10acsq, iPTF13cuf) are excluded also in the rise time analysis. The available pre-peak photometry does not allow a reliable measurement of the rise time if the difference in magnitude covered during the rise is too small, or if the photometry is taken during a too short time interval. For the magnitude interval (Δm) and time interval (Δt) covered by n pre-peak detections, we therefor exclude any SN having $\Delta m < 0.60$ mag and $n/\Delta t > 0.40$ d^{-1}. This re-

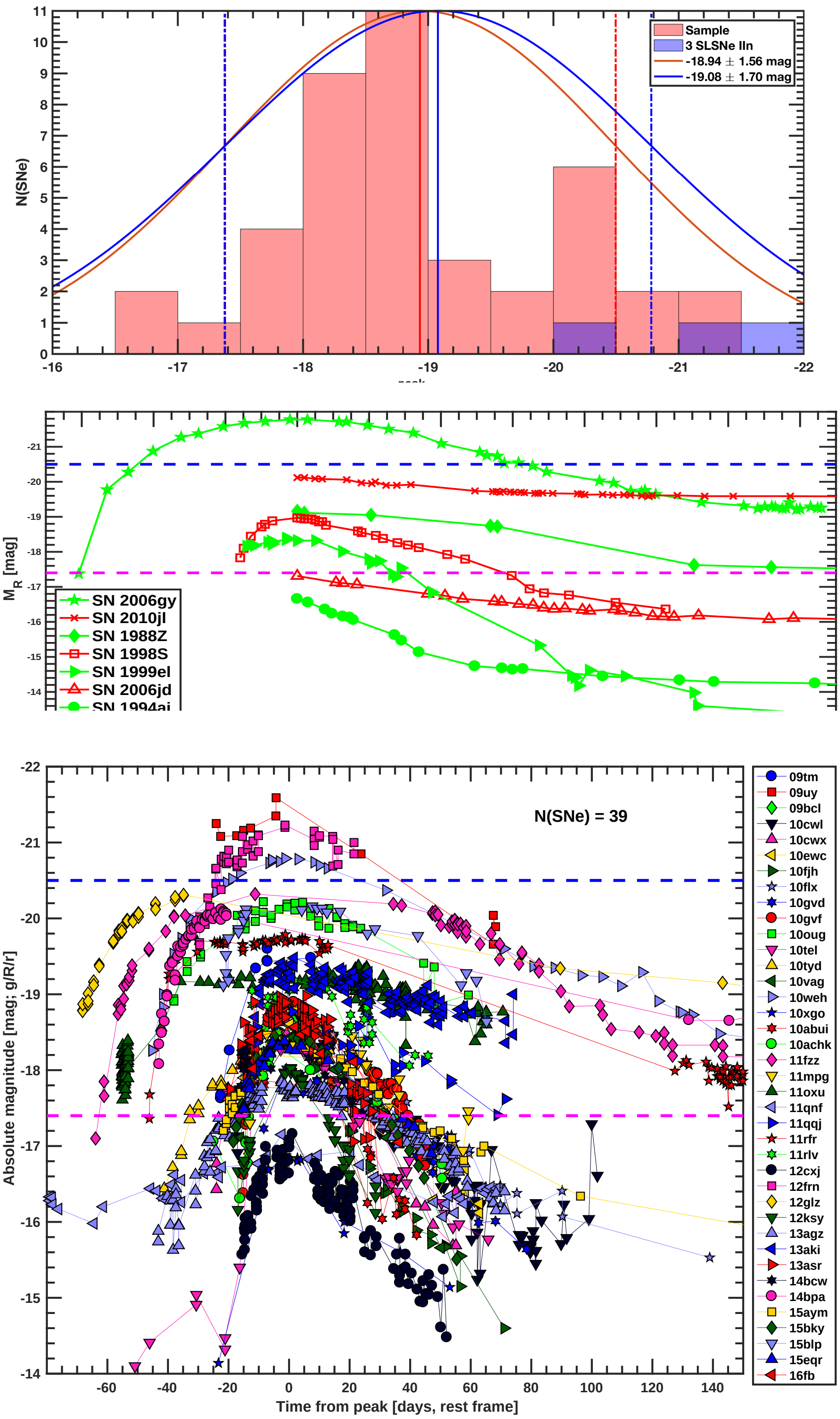

Figure 6 Top panel: Histogram for the peak absolute magnitudes of our 42+3 SNe IIn, overplotted with the best-fit Gaussian distributions as identified with GMM. The Gaussian describing the distribution for the sample of 42 SNe is shown in red, the Gaussian for the sample 42 SNe IIn + 3 SLSNe IIn is shown in blue. The bulk ($\sim$ 83%) of the SNe IIn from our sample lies between -17.4 mag and -20.5 mag, i.e., within 1σ of the mean when assuming a Gaussian distribution. Central panel: Some well-studied SNe IIn from the literature, showing photometry of SN 1988Z (Aretxaga et al. 1999), SN 1994aj (Benetti et al. 1998), SN 1998S (Liu et al. 2000), SN 1999el (Di Carlo et al. 2002), SN 2006gy (Smith & McCray 2007b), SN 2006jd (Stritzinger et al. 2012), and SN 2010jl (Fransson et al. 2014). Bottom panel: The absolute magnitudes of our SN IIn sample (here: the 39 SNe with determined peak epochs) as a function of time since light-curve peak, with -17.4 mag shown as a magenta dashed line) and -20.5 mag shown as a blue dashed line. No K-corrections were applied in these plots.

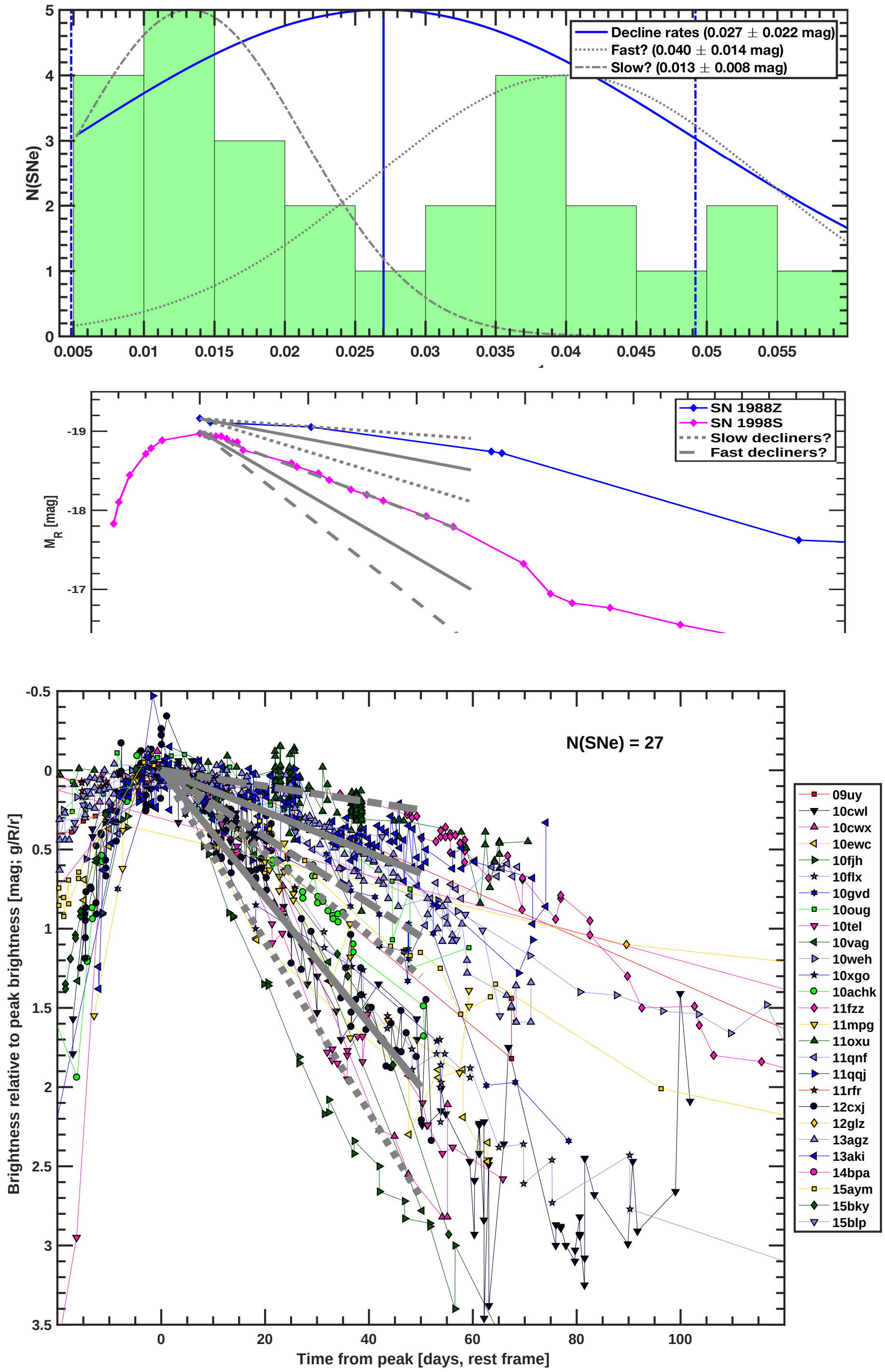

Figure 7 Top panel: Histogram for the decline rates between 0 and 50 d post maximum brightness for 27 of our SNe IIn. A single Gaussian (identified using GMM with BIC) describing the whole population is shown in blue, but our SNe IIn might possibly divide into fast (grey dash-dot lines) and slow (grey dash lines) decliners, with slopes $0.040 \pm 0.014\,\mathrm{mag\,d^{-1}}$ and $0.013 \pm 0.008\,\mathrm{mag\,d^{-1}}$, respectively (suggested by GMM with AIC). Central panel: the two possible groups of SNe IIn (slow and fast decliners) compared to the prototypical slow and fast decliners from the literature (SN 1988Z, Aretxaga et al. 1999; SN 1998S, Liu et al. 2000). Bottom panel: The light curves of the 27 of our SNe IIn with measured decline rates (between 0 and 50 d), scaled to match at peak, with the two different decline rates overplotted; fast (grey dash-dot lines) and slow (grey dash lines) decliners.

moves PTF10abui, PTF10flx, PTF11rlv, PTF11qqj, iPTF14bcw and iPTF16fb from the rise time analysis.

To make a rising light-curve template for rise-time measurements, we considered SNe from our sample with $z < 0.075$, having the first detection within 4 d of the last upper limit (in the observer's frame) and this first detection having $m_R > 21$ mag. At $z = 0.075$, this means $M_R \gtrsim -16.5$ mag. This gives the rising light-curve template candidates PTF10cwx, PTF10tel, PTF10tyd, PTF11qnf, and iPTF13agz. We choose PTF10tyd as our template owing to it having the lowest $\chi^2_{\mathrm{d.o.f.}}$ for a fitted t^2

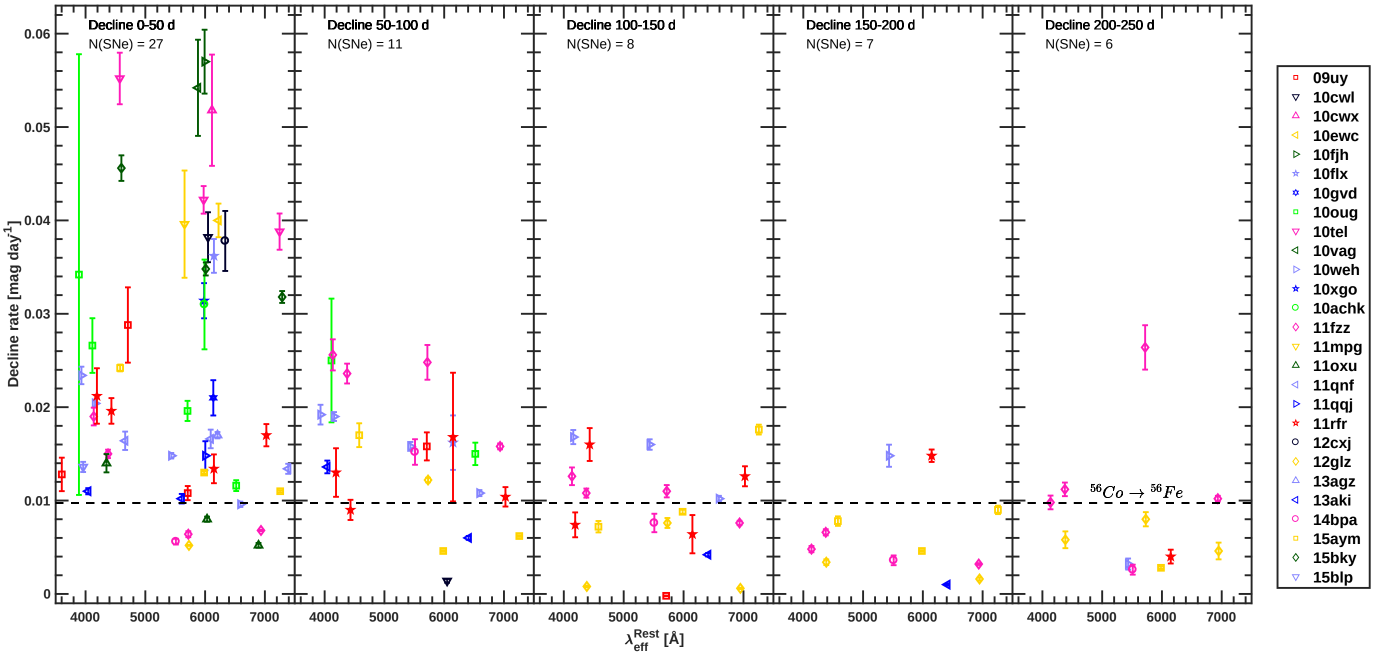

Figure 8 Decline rates 50–250 rest-frame days (past the peak time given in Table 5) of 27 of the SNe in our sample. For reference, the decay rate of ^{56}Co $\rightarrow^{56}$ Fe (0.0097 mag d^{-1}) is shown as a dashed black line. The number of unique SNe in each panel is given as N(SNe).

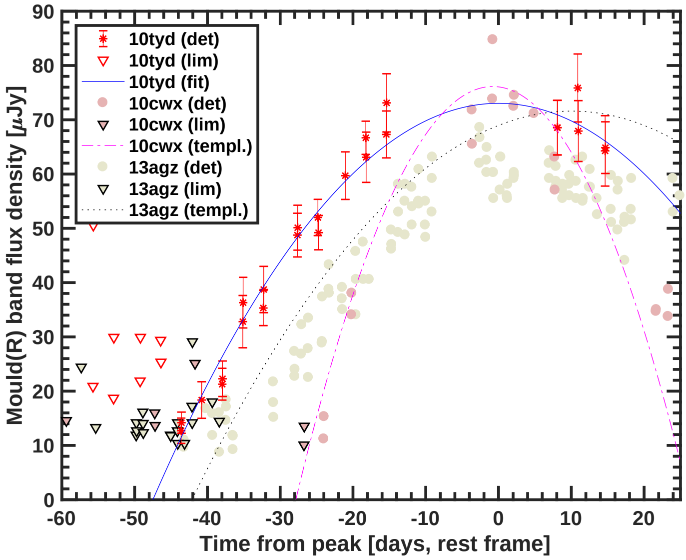

Figure 9 R-band light curve of PTF10tyd (flux-density scale), with weighted fit of the $\propto t^2$ template shown along with the rise template candidates PTF10cwx and iPTF13agz. For comparison, the $\propto t^2$ curves for PTF10cwx and iPTF13agz are also shown, with scale, stretch, and shift parameters as found in Sect. 4.3 applied.

power law. A least-squares fit to the PTF10tyd rising light curve (flux-density scale) gives the rest-frame template with the rise time $\Delta t = 47.5$ d (Fig. 9) for the power-law model

$$L(t) = L_{\rm peak} \left[1 - \left(\frac{t - t_{\rm peak}}{\Delta t} \right)^2 \right], \qquad (1)$$

where $L_{\rm peak}$ is the peak luminosity from the fit, Δt is the time from 0 to peak luminosity, and $t_{\rm peak}$ is the time of the peak luminosity (Ofek et al. 2014b, their Eq. 5). This template will be stretched, scaled, and shifted in order to fit the other SNe in our sample (see Fig. 10). For demonstration, in Fig. 9 we also show the PTF10tyd template stretched, scaled, and shifted to the light curves of template candidates PTF10cwx and iPTF13agz.

In Fig. 10 we have converted pre-peak AB magnitudes of the SN to flux density as in Sect. 4.1 and normalised the flux-density values to peak brightness. We then stretch the light-curve data points in time by applying a multiplicative factor, scale their position in flux density (additively), and shift their position in time (additively) to minimise the distance (in a LSQ sense) of the light-curve data points to the power-law template. When this is done, the derived stretch value is used to compute the rise time of the input SN (as $t_{\rm rise} = \Delta t_{\rm PTF10tyd}/{\rm stretch}$). A MC experiment is done to generate new light-curve data points within the light-curve error bars. The light-curve stretch, scale, and shift operations are then repeated to estimate the uncertainty of the stretch value.

For the cases where the obtained $\propto t^2$ template fit ends up inconsistent (i.e., brighter) than an upper limit observed before the first detection, the time of that upper limit is assumed as an approximation of the "start of rise" epoch. In such cases, as an estimate of the uncertainty we assume the time between the upper limit and the first detection. For the special case of PTF10tel (Ofek et al. 2013), with its detected photometric activity before the start of rise, we adopt the explosion epoch given by Ofek et al. (2013) as the "start of rise" epoch. The derived rise times (in the rest frame) are presented in Table 5.

We plot the histogram of the rise times in the top panel of Fig. 11. The SN IIn population is characterised by a large range of rise times, and a GMM test (Sect. 4.1) shows a significant division (for both AIC and BIC) into two groups: fast-rising SNe IIn with rise times of 20 ± 8 d (magenta lines in Fig. 11) and slow-rising SNe IIn with rise times of 50 ± 15 d (blue lines). PTF11qnf, where we found a rise time to peak of 133 d (Table 5) and a faint ($\rm M_r \approx -17$ mag) peak, is an outlier not included in

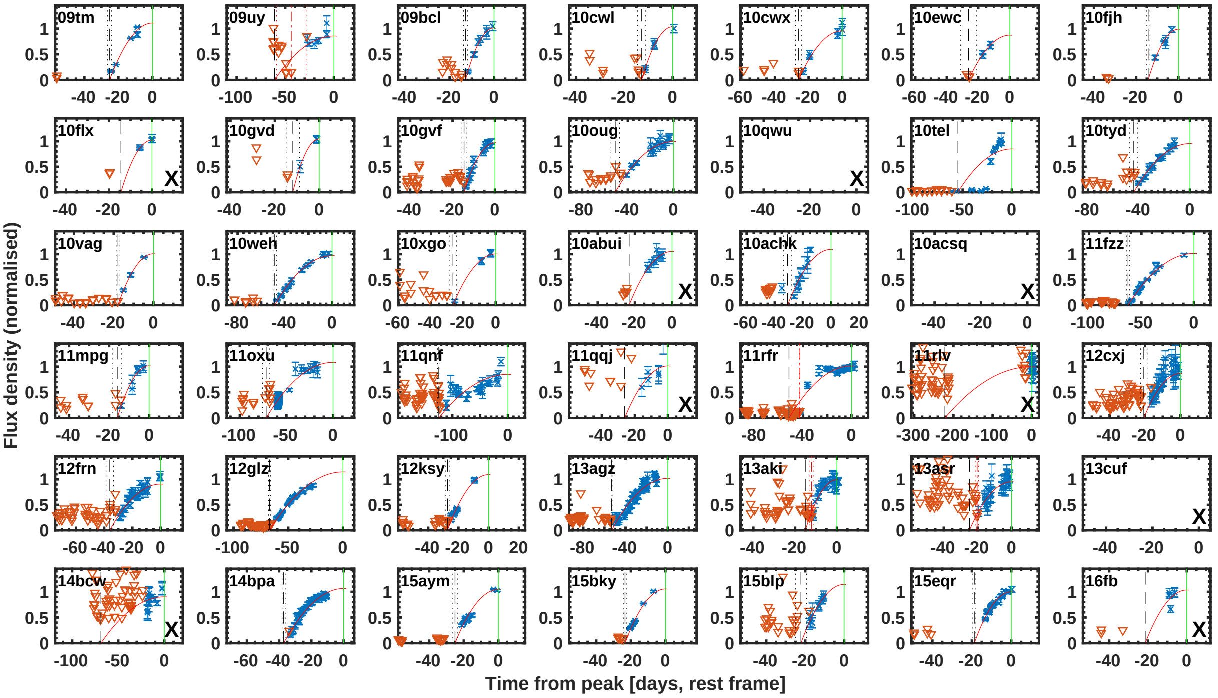

Figure 10 Fits of the $\propto t^2$ template to determine the rise times of the SNe in our sample. Photometric bands are as specified in Table 5. The black dashed vertical line shows where the $\propto t^2$ template reaches 0 flux density (with 1σ uncertainties given as black dotted lines). The red dashed vertical line shows where the explosion epoch estimate is based on the occurrence of an upper limit inconsistent with the $\propto t^2$ template (with uncertainties given as red dotted lines). The SNe with "X" in their plots are not used for the rise-time measurements, according to criteria given in Sect. 4.3. For the SNe with peak-time error > 10 d (PTF10qwu, PTF10acsq, iPTF13cuf), our method does not allow any rise-time determination; these SNe are not shown.

this rise-time GMM analysis. PTF11qnf might have been a SN impostor (Sect. 5.3).

The literature about SNe IIn already showed examples of fast-rising SNe IIn like SN 1998S and slow-rising SNe IIn like the SLSN Type IIn SN 2006gy. These two SNe are displayed in the central panel of Fig. 11 and the rising portions of their light curves are compared to the two rise-time ranges we found in our sample. We overplot all our SNe IIn with measured rise times in the bottom panel of Fig. 11, to further illustrate the variety of rise-time values and the relatively similar light-curve shapes. We particularly note the erratic light curve of PTF11qnf as well as the precursor activity prior to the start of rise for PTF10tel (as analysed by Ofek et al. 2013 and compared to SN 2009ip by, for example, Pastorello et al. 2018 and Smith et al. 2014). In Sect. 5 we will further discuss these events.

4.4. *Correlations between light-curve properties*

Having measured the main light-curve-shape parameters, we proceed to check if these quantities are somehow correlated in our sample. Ofek et al. (2014a) suggests a correlation between rise time and peak luminosity, based on the assumption of the SN shock breaking out in the CSM. This was studied observationally by Ofek et al. (2014b), inferring a possible correlation. From analytical models, Moriya & Maeda (2014) instead indicate that no strong dependence on rise time should be seen for the peak luminosity (shock breakout does not have to occur in the CSM of all SNe IIn.). In Fig. 12 we use the peak luminosities obtained from absolute r/R-band magnitudes M_r with

$$L(M_r) = (3.04 \times 10^{35}) \times 10^{(-0.4\ M_r)}\,\mathrm{erg\,s^{-1}} \tag{2}$$

based on solar bolometric values and, following Ofek et al. 2014b and Nyholm et al. 2017, neglecting bolometric corrections. A unweighted Spearman correlation test for the SNe plotted in Fig. 12 gives the correlation coefficient $p = 0.23$, corresponding to a significance of $\sim 1.19\sigma$. We report the significance for a given correlation coefficient p as $\sqrt{2} \times \mathrm{erf}^{-1}(1-p)$, using a two-sided tail of the normal distribution. Excluding the possible SN impostor PTF11qnf (Sect. 5.3) gives $p = 0.08$ ($\sim 1.8\sigma$). If a correlation between rise time and peak luminosity exists at all, it is weak. Using a bootstrap technique, Ofek et al. (2014b) claimed a significance of $\sim 2.5\sigma$ for their sample of 15 SNe IIn (12 of which are in our sample). With our method, we find a significance of $\sim 1.75\sigma$ for this Ofek et al. (2014b) sample. Finding a weaker significance for the correlation with our larger sample (33 SNe) suggests that the correlation Ofek et al. (2014b) found might have suffered from small-number statistics.

In Fig. 13 (left panel) we find a correlation with $p = 0.0037$ ($\sim 2.9\sigma$) for rise time versus decline rate. This shows that slowly rising SNe IIn are also slow decliners, and fast risers are fast decliners. The empty upper-right corner of the decline rate vs. rise time plot of Fig. 13 shows that we do not see any SNe having both a slow rise and a fast decline. For peak absolute magnitude versus decline rate (Fig. 13, right panel), we obtain $p = 0.0065$ ($\sim 2.7\sigma$), suggesting that the more luminous SNe IIn decline slower. This is somewhat comparable to the Phillips relation (Pskovskii 1977; Phillips 1993) between peak magnitude and decline rate for SNe Ia, but less tight in the SN IIn case. These correlations for SNe IIn can be discerned in the bottom panel of Fig. 6.

As a check, we investigate the presence of bias by looking for correlations between rise or decline rates and the peak *apparent*

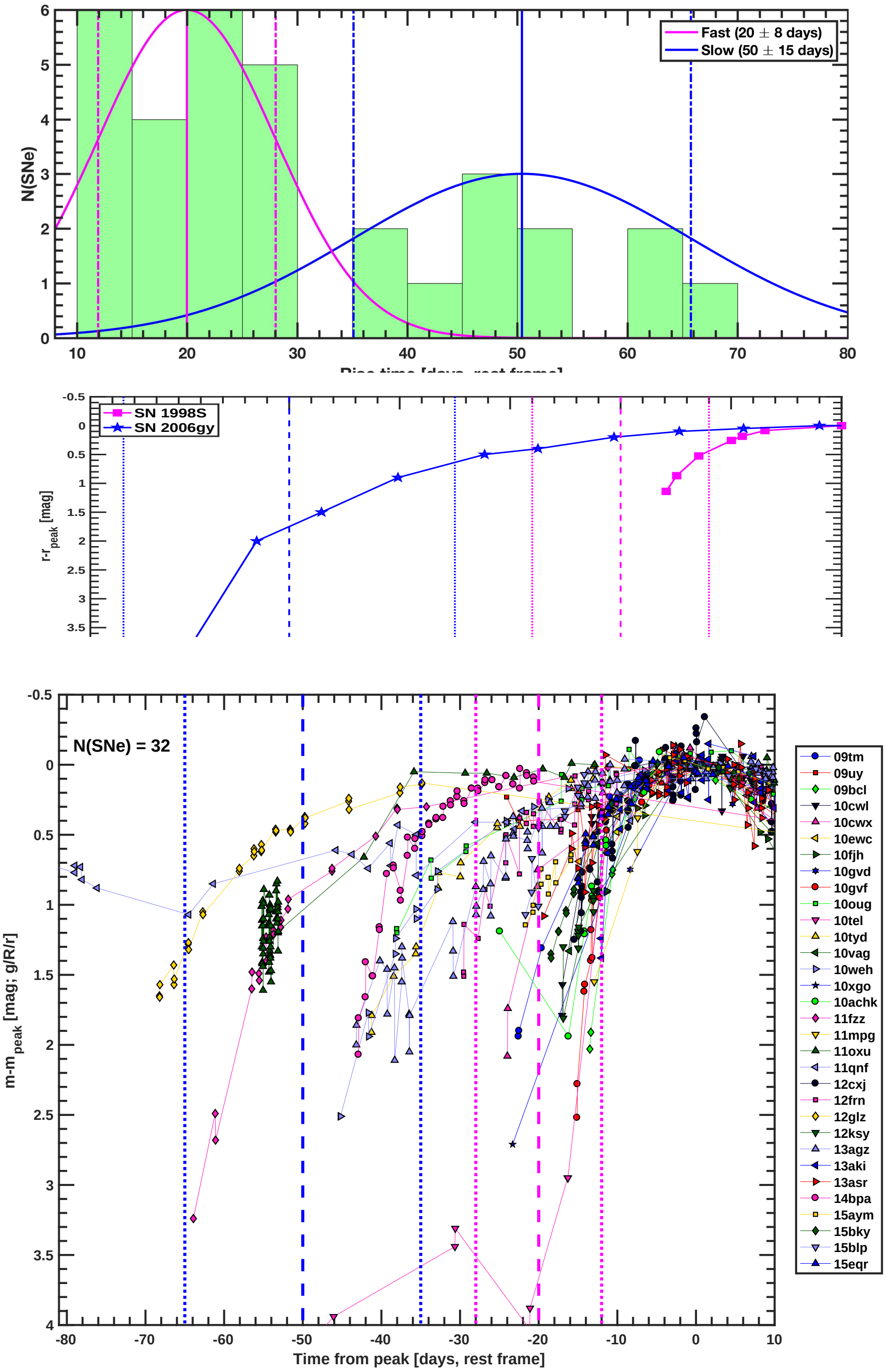

Figure 11 Top panel: Histogram for the rise times for 32 of our SNe IIn. For reasons discussed in Sect. 5.3, we excluded PTF11qnf from this analysis. Our SNe IIn are divided into fast (magenta lines) and slow (blue lines) risers, with rise times 20 ± 8 d and 50 ± 15 d, respectively (as identified with GMM). Central panel: the two groups of SNe IIn (slow and fast risers) compared to two well-known slow and fast risers from the literature (SN 2006gy, Smith & McCray 2007b; SN 1998S, Liu et al. 2000). Bottom panel: The light curves of the 32 SNe in our sample with well-determined peak times matched at peak brightness, with the rise-time ranges overplotted.

magnitudes of the SNe IIn. Such a correlation might indicate bias affecting the correlations discussed above. The decline rate against peak apparent magnitude gives $p = 0.28$ ($\sim 1.1\sigma$). The rise time against peak apparent magnitude gives $p = 0.52$ ($\sim 0.65\sigma$). The absence of a correlation in both cases suggests that the correlations with absolute magnitude are real.

4.5. Colour evolution

Only a small number of SN IIn sample studies have considered the colour evolution of the SNe IIn in a collective fashion. Compilations of colour evolution of SNe IIn were presented by Taddia et al. (2013) and de la Rosa et al. (2016), based on their respective samples. In Fig. 14, we present the $g - r$ and $g - i$

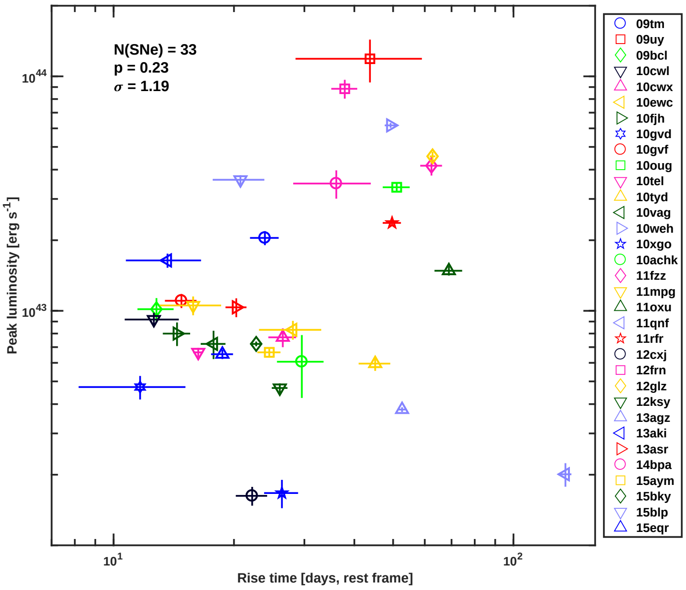

Figure 12 The rise times and peak luminosities for 33 of the SNe in the sample, using measurements described in Sect. 4.3, following the investigation by Ofek et al. (2014b). The photometric band used for each SN is given in Table 5. The Spearman correlation coefficient p, along with the corresponding significance σ and the number of SNe, N(SNe), are shown.

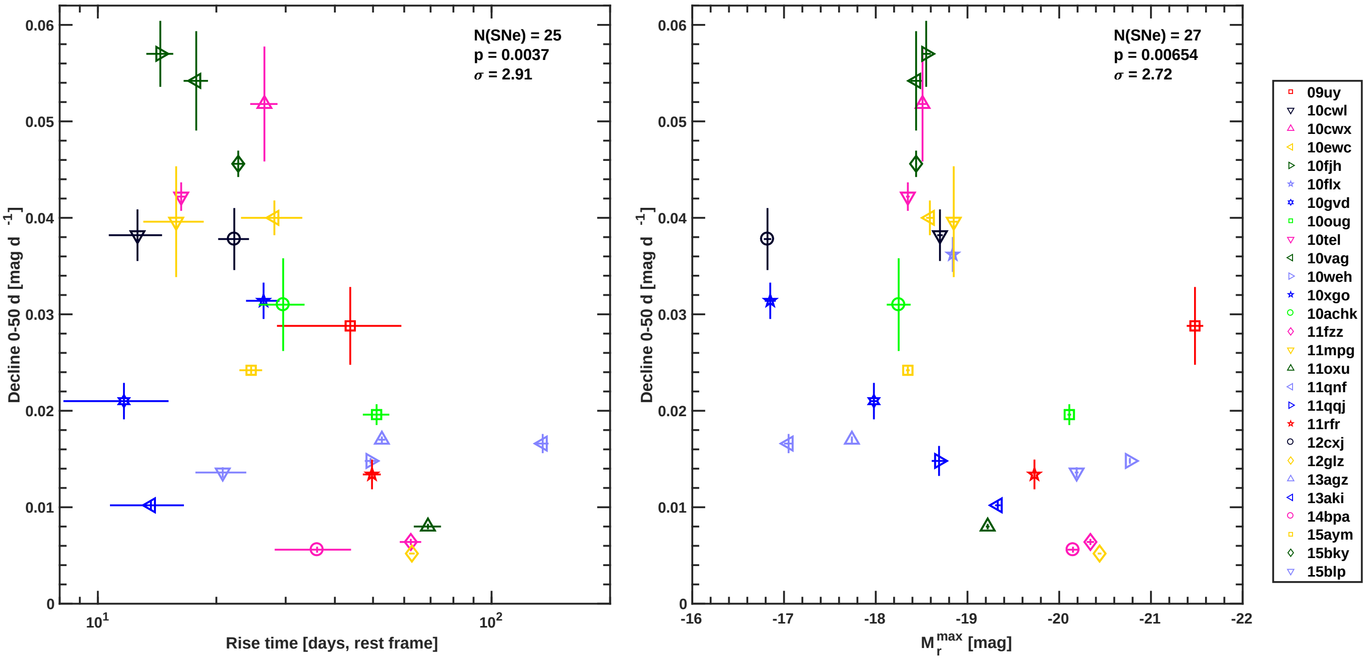

Figure 13 Examination of possible correlations between decline rates or rise times and peak magnitudes of the sample SNe (Sect. 4.4). Photometric bands are as specified in Table 5. In each panel the Spearman correlation coefficient for each plot p, along with the corresponding significance σ and the number of SNe, N(SNe), are shown.

colour evolution for 22 of our SNe IIn with respect to the light-curve peak epochs. The magnitudes used were corrected for extinction as described in Sect. 3.1.

For comparison, we also plot the $g-r$ and $g-i$ colours of the slowly evolving SNe IIn 2005ip and 2006jd (photometry from Stritzinger et al. 2012) and the rapidly evolving SNe IIn 2006aa and 2008fq (photometry from Taddia et al. 2013). The colour curves for these four events from the literature have been computed using the MW and host extinctions and peak epochs given in the respective papers. The evolution of the $g-i$ colour is rather monotonic for the sample as a whole, albeit with some spread. SNe 2006aa and 2008fq have $g-i$ colour evolution encompassing most of our sample SNe, while SNe IIn with the slower $g-i$ colour evolution of SNe 2005ip and 2006jd are not seen among our 22 plotted SNe. The $g-i$ colour evolving toward the red for the majority of the SNe reflects their decreasing blackbody continuum temperatures. The $g-r$ colour evolution is likely affected by the evolution of the Hα emission line (with a line centre within the SDSS r filter for $z \lesssim 0.065$, where 7 of the 22 SNe in Fig. 14 are located).

The small spread in colours suggests that the colour corrections applied (Sect. 3.1) are without large errors. Exceptions are the $g-r$ colour of iPTF15eqr and the $g-i$ colour of PTF11qnf. In the case of PTF11qnf, a possible SN impostor, its colour index and its host $E(B-V)$ will be discussed in Sect. 5.3.

Our analysis of rise and decline behaviour (Sect. 4.4) as well as the luminosity function (Sect. 4.6) is based on r/R-band photometry as far as possible, but when the r/R-band is not available, we used the g-band instead. This is the case for four of our SNe (Table 5). Via linear interpolation between epochs surrounding time of peak, we find the colours of each SN at peak. The $g-r$ colour index at peak of the SNe IIn is $g-r = 0.06 \pm 0.21$ mag and $g-i = 0.13 \pm 0.46$ mag. This is consistent with $g-r \approx 0$ mag and $g-i \approx 0$ mag around peak brightness, and it indicates that our use of g-band for four SNe in our analysis should not affect our conclusions.

4.6. Luminosity function

The observed luminosity function (see Fig. 6, top panel) of the SNe in our sample is affected by Malmquist bias (Malmquist 1922). This means that SNe intrinsically luminous at peak (thus easier to detect in a magnitude-limited survey like PTF/iPTF) are over-represented compared to the intrinsically less luminous SNe. To reduce the impact of the Malmquist bias on our estimated luminosity function, we use the bootstrap method described by Richardson et al. (2014) as implemented by Taddia et al. (2019).

Figure 15 (upper panel) shows the peak absolute magnitude as a function of distance modulus (μ) for our 42 sample SNe. PTF12cxj with $M_r^{\max} = -16.82$ mag is the faintest SN in the sample and the dashed diagonal line represents the typical limiting magnitude of the PTF/iPTF survey under good conditions, $m_R \approx 21$ mag. This indicates that our sample satisfactorily represents the SN IIn population up to $\mu \approx 37.8$ mag ($z \approx 0.08$). This is consistent with the sample redshift distribution shown in Fig. 3. We consider the peak-magnitude distribution observed at $\mu < 37.8$ mag as intrinsic in the intervals $-17.8 < M_r^{\max} < -16.8$ mag and $-18.8 < M_r^{\max} < -17.8$ mag, respectively, and randomly generate the peak magnitudes of the missing SNe with $-17.8 < M_r^{\max} < -16.8$ mag in the interval $37.8 < \mu < 38.8$ mag based on these intrinsic distributions. The same random generation of missing SNe is repeated for the more distant μ intervals, and are shown as empty red diamond symbols in Fig. 15 (upper panel). The observed luminosity function of the SN sample is $M_{\text{peak}} = -18.96 \pm 1.11$ mag whereas the Malmquist-bias-compensated luminosity function has $M_{\text{peak}} = -18.60 \pm 1.25$ mag (the given spread is 1σ); see Fig. 15.

The sample of 42 SNe IIn was selected from a body of SNe IIn all deemed to have $M_{\text{peak}} > -21$ mag (Sect. 3) and thus not being SLSNe according to the traditional (Gal-Yam 2012) criterion. In the study by Richardson et al. (2014), SNe IIn with $M_{\text{peak}} < -21$ mag were also included, so to facilitate a comparison of results, we repeated the above Malmquist-bias correction for the 45 SNe IIn encompassing the main sample of 42 SNe IIn and the 3 SLSNe IIn (PTF10heh, PTF12mkp, and iPTF13do) introduced in Sect. 3. The observed luminosity function of this extended SN sample is $M_{\text{peak}} = -19.10 \pm 1.21$ mag whereas its bias-corrected luminosity function is $M_{\text{peak}} = -18.73 \pm 1.35$ mag. Richardson et al. (2014) found a bias-corrected distribution of $M_{\text{peak}} = -18.53 \pm 1.36$ mag, which is similar to our result.

Richardson et al. (2014) applied a K-correction based on spectra of SN 1995G (slowly declining) and SN 1998S (rapidly declining) in their calculations. When we include our K-corrections and their uncertainties (using Eqs. A.1 and A.2; for any $z > 0.31351$, we assume the K-correction for $z = 0.31351$) the Malmquist-bias-compensated luminosity function becomes $M_{\text{peak}} = -18.72 \pm 1.32$ mag. Here, we assume that all the SNe were observed in the r/R-band. For the extended SN sample (including the 3 SLSNe IIn) and including K-corrections, we find the Malmquist-bias-corrected luminosity function $M_{\text{peak}} = -19.18 \pm 1.32$ mag. The means of the derived K-corrected distributions are more luminous than the ones without K-correction by 0.12 mag and 0.45 mag, respectively, but consistent within 1σ.

4.7. Host galaxies

The host galaxies of our sample of SNe can be expected to have a wide range of absolute magnitudes, since the SNe were found in an untargeted search not giving priority to any special galaxy type. In earlier SN searches, nearby galaxies with lively star formation were sometimes targeted to increase the chance of finding SNe (Anderson & Soto 2013). The sample of SNe IIn whose environments were studied by Taddia et al. (2015) has a bias toward hosts being large spiral galaxies. Here, we examine whether our sample SNe are hosted by galaxies covering a different range of absolute magnitudes than the hosts in the Taddia et al. (2015) sample.

From a study of the properties of PTF/iPTF SN host galaxies (Schulze et al., in prep.), we collected g-band absolute magnitudes of the host galaxies of our 42 sample SNe. Schulze et al. obtained the total flux of a galaxy in the different SDSS filters via a curve-of-growth analysis. For galaxies outside the SDSS field, Pan-STARRS images were used instead. In the case of PTF09uy and PTF10qwu the measurements in Perley et al. (2016) were used. The absolute magnitudes were obtained by modelling their spectral energy distributions with `Le PHARE` (Arnouts et al. 1999; Ilbert et al. 2006). The host absolute magnitudes (largely consistent with Petrosian magnitudes, Petrosian 1976) are given in Table 4.

We limited our comparison to the Taddia et al. (2015) SN IIn sample hosts also in the SDSS field, obtaining their Petrosian magnitudes under the *PhotoTag* section of the SDSS DR15 Object Explorer web pages, considering galaxies with `petroMagErr_g` < 0.2 mag. This gave 23 galaxies. We used Schlafly & Finkbeiner (2011) to get the foreground extinctions and the redshifts from Taddia et al. (2015) with our infall-compensation method (Sect. 3.1) to calculate absolute magnitudes. For the redshifts ($\lesssim 0.02$) of these literature SN hosts, K-corrections are generally small ($\lesssim 0.2$ mag; Chilingarian et al. 2010) and can be neglected. The cumulative distribution functions of the host galaxy g-band absolute magnitudes are shown in Fig. 16. For completeness, we note that two SNe IIn from the Taddia et al. (2015) sample (SNe 1997ab and 2007va) were hosted by dwarf galaxies; these galaxies did not pass our `petroMagErr_g` requirement. The 42 sample SN host galaxies have $-21.6 < M_g < -12.8$ mag (8.8 mag interval). For the 23 SN host galaxies from the Taddia et al. (2015) sample, the absolute magnitudes are $-21.6 < M_g < -17.0$ mag (4.6 mag interval). The host galaxies of the SNe from our untargeted sample thus cover a range of absolute magnitudes about 4 mag wider (toward the fainter end) than the SN host galaxies from the targeted searches for which we have reliable SDSS photometry, also having a different distribution.

The luminosity-metallicity relation by Tremonti et al. (2004, their Fig. 5) shows that the spread in M_g for our sample hosts in Fig. 16 corresponds to a wide range of global galaxy metallicities, from above solar metallicity (up to approximately 12 +

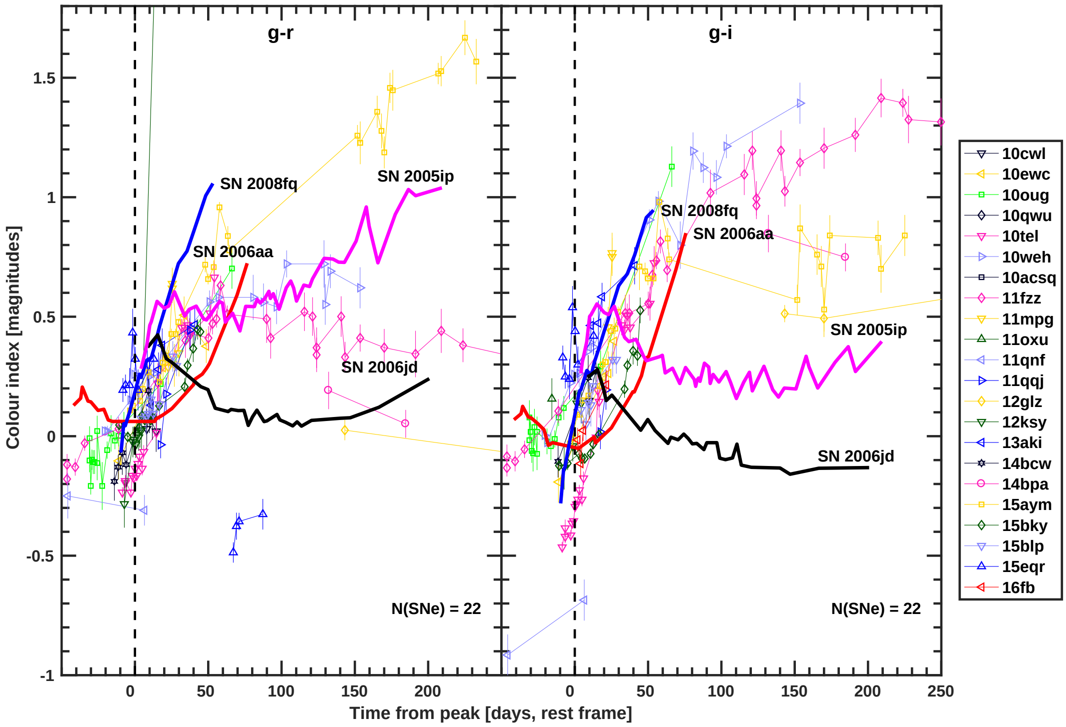

Figure 14 The evolution of $g-r$ and $g-i$ colours for 22 SNe in the sample. Host and MW extinction have been removed (Sect. 3.1). The thick, vertical black dashed line shows the light-curve peak epoch (Sect. 4.3). Lines are drawn between data points to guide the eye. For clarity, colour data points with uncertainties $>$ 0.1 mag are not shown. For comparison, SNe IIn 2005ip, 2006jd (Stritzinger et al. 2012), 2006aa, and 2008fq (Taddia et al. 2013) have their colour curves shown with bold lines.

$\log\,[\frac{\mathrm{O}}{\mathrm{H}}] \approx 9$ on the scale of Kobulnicky & Kewley (2004)), to $12+\log\,[\frac{O}{H}] \lesssim 8$ (i.e., subsolar) for the fainter end of our distribution ($M_g \gtrsim -16$ mag). The work by Habergham et al. (2014), Taddia et al. (2015), Anderson et al. (2015), and Galbany et al. (2018) on SN IIn environments shows that studies of global properties of host galaxies are insufficient when detailed conclusions are to be drawn about SNe IIn and their progenitor channels[3], but it is clear that an untargeted search like the one used to build our SN sample has the potential to probe a more representative part of the galaxy population.

4.8. Interpretation using models

As discussed in Sect. 4.4, Ofek et al. (2014a) claim the possible existence of a correlation between the rise time and the peak luminosity of SNe IIn, assuming that the CSM close to the progenitor star is dense enough to allow shock breakout (SBO) to happen in the CSM. In Sect. 4.4, we saw that such a correlation hardly exists.

As an alternative to studying the relations between peak absolute magnitude and rise time or decline rates (Sect. 4.4), the relation between peak absolute magnitude and overall duration can also be considered. The location of the SNe in this duration-luminosity phase space (DLPS) can give insights into the mechanisms of the SNe. Using our spline fits (Sect. 4.1) we can measure the duration of the light curves as the time it takes for the light curve to rise and decline 1 mag relative to its peak (as in Villar et al. 2017). This duration measurement is possible for 31 of our spline-fitted SN light curves in Fig. 5.

A comprehensive exploration of the DLPS for different astronomical transients was done by Villar et al. (2017), who used the MOSFiT (Modular Open Source Fitter for Transients) code (Guillochon et al. 2018) to explore the locations in the DLPS occupied by transients driven by different mechanisms (such as CSI) occurring under wide but realistic parameter ranges. Using the analytical models based on Chatzopoulos et al. (2012) for the SN-like CSI transients (with both wind-like and shell-like CSM profiles) and the model by Ofek et al. (2014a) for SBO interacting transients, Villar et al. (2017) calculated 68th and 90th percentile contours for the DLPS populated by CSI-driven transients. The CSM mass in all models was picked from the range 0.1–10 $M_{\odot}$, sampled log-uniformly. In Fig. 17 we compare our sample SNe to the DLPS percentile contours by Villar et al. (2017). The slight overlap of the contours in some places for the SN-like transients is due to the contours being generated based on only 1000 MC realisations (Ashley Villar, personal communication). We also plot SLSNe IIn PTF10heh and PTF12mkp (Sect. 3). For comparison, we also did spline measurements (as in Sect. 4.1) for photometry of SNe 1998S (Liu et al. 2000), 2006gy (Smith et al. 2007a), and 2009ip (2012B event, Graham et al. 2014) to include them in Fig. 17 for comparison. A unweighted Spearman test for the 31 sample SNe IIn plotted in Fig. 17 gives $p = 0.0084$, corresponding to a significance of $\sim 2.6\sigma$. A correlation like this (more luminous SNe IIn generally evolving more slowly) could be expected, based on the investigation presented in Fig. 13. It is noteworthy that in Sect. 4.4, we found a correlation (at 2.7σ) between peak brightness and decline rate, but no correlation ($\sim 1\sigma$) between peak brightness and rise time. The overall slower evolu-

---

[3] Spearman correlation tests (unweighted) for SNe peak absolute magnitudes, rise times, and decline rates as a function of M_g of the host galaxies (c.f. Sect. 4.4) give significance levels of $\sigma \lesssim 1$, i.e., no correlation can be seen.

tion of more luminous SNe IIn therefore seems to be dictated by the decline rates of the SNe.

In Fig. 17 we see that 18 of the sample SNe IIn reside within both the SBO 68$^{\rm th}$ percentile and the wind-like 68$^{\rm th}$ percentile, suggesting that either model could explain these SNe. At $M \lesssim -20$ mag, we see six SNe outside the SBO 90$^{\rm th}$ percentile but still inside the wind-like 68$^{\rm th}$ percentile, making it less likely that they are SBO-driven SNe IIn. None of the SNe plotted (not even the comparison events SN 2006gy, PTF10heh, or PTF12mkp) reside in the DLPS region only covered by the shell-like model realistions. While these three so-called SLSNe could arise from SN ejecta interacting with a shell-like CSM, it seems not to be a necessary assumption.

The DLPS in Fig. 17 display a noticeable clustering of events with durations between 20 d and 40 d and peak magnitudes between ~ -18 and ~ -19, whereas the more luminous ($M < -20$ mag) and durable events are rarer. Observationally, more durable and luminous events should be easier to find and monitor, also at higher redshifts. This might indicate that the less luminous and less durable SNe IIn are intrinsically more common. This can be interpreted such that progenitors with a relatively lower mass-loss rate toward the end of their existence dominate the zoo of SN IIn progenitors. A rapidly declining SN IIn likely has a less dense CSM, whereas a slowly declining SN IIn should have an extended dense CSM. The differences in extent and density of the CSM suggest a difference in the mass-loss histories of SN IIn progenitors, with the progenitors of more durable and luminous SNe IIn having enhanced mass loss for centuries before the SN explosions, while the fainter and briefer SNe IIn only have stronger mass loss during decades before the SN (Moriya et al. 2014).

5. Discussion

In this section, we will discuss the contents of our sample and put it in the context of SNe IIn from the literature. We examine what could be contaminating our sample in terms of unrelated astronomical transients, and we evaluate sources of errors. Further, we discuss some of our individual SNe and compare them to SNe in the literature with respect to SN impostors, light-curve bumps, and flat light-curve maxima.

5.1. Possible contaminants in the sample?

Transients showing SN IIn spectral signatures are usually understood to involve a supergiant star having an outburst (destructive or not) inside a substantial CSM. There are, however, other mechanisms that can mimic the SN IIn signature and which could possibly contaminate our sample. Here, we will discuss two such mechanisms.

Under some circumstances, an active galactic nucleus (AGN) can appear like a SN IIn both spectroscopically and photometrically. For example, an early label put on SNe 1987F and 1988I (later classified as SNe IIn) was "Seyfert 1-like" (Filippenko 1989). The erratic photometric behaviour of an AGN (caused by changes in accretion rate of its supermassive black hole) can lead to variability episodes (e.g., Graham et al. 2019) with duration and absolute magnitude comparable to some SNe IIn. Most of the SNe in our sample are located off-centre in their host galaxies. Vetting The Million Quasars catalogue (version 5.2, 2017 August) compiled by Flesch (2015) shows that no known AGN is found in the catalogue within 5$''$ of the SN positions. This suggests that the transients in our sample SNe are not AGN in outburst mimicking SNe IIn.

Some thermonuclear SNe have been observed showing spectra with SN IIn-like Balmer lines superimposed on ordinary SN Ia spectra (e.g., Hamuy et al. 2003). These SNe Ia-CSM have been proposed to happen when white dwarfs explode inside the CSM of its nondegenerate binary companion (see Silverman et al. 2013, and references therein). In simulations by Leloudas et al. (2015) it was shown that SNe Ia-CSM can be mistaken for genuine SNe IIn under some circumstances. Leloudas et al. (2015) shows that a SN Ia (of typical peak magnitude $M \approx -19$) can be hidden under an apparent SN IIn spectrum if the CSI is strong and the peak magnitude of the SN IIn is $M \approx -20.9$. In this interval, our sample contains PTF12frn (Table 5). We caution that this SN might have an overestimated host extinction (Sect. 3.1). PTF12frn was a part of the feeder sample for the Silverman et al. (2013) sample, but study of its spectra made them conclude that it was not a SN Ia-CSM. It therefore seems likely that none of our sample SNe are SNe Ia-CSM.

5.2. Sources of errors

Some of the assumptions made while measuring the light-curve properties could affect our analysis and conclusions. Sources of error important for absolute magnitudes and colours are the extinction corrections, distances, and the bolometric correction for the SNe. The values we obtain for SN decline rates and rise times are not affected by these.

No comprehensive study of bolometric corrections (BC) for SNe IIn has yet been done. The Balmer emission lines in their spectra as well as the infrared contributions from dust (Fox et al. 2013) makes their BC hard to estimate. For blackbody temperatures between 7500 and 11,000 K, the bolometric correction of our Mould R-band filter is $-0.6 < BC < -0.06$ mag (Ofek et al. 2014a, footnote 22). These BC values for SNe IIn are adopted by Moriya & Maeda (2014). For practical reasons (and following Ofek et al. 2014b and Nyholm et al. 2017), we have been using $BC = 0$ mag in our analysis with the R/r and g bands, and this likely introduces an error.

Several samples of CC SNe (e.g., Valenti et al. 2016; Taddia et al. 2015, 2019) show host colour excess in the range $0 \lesssim E(B-V) \lesssim 0.4$ mag. In the literature compilation for SN Ia host galaxies by Cikota et al. (2016), the absorption-to-reddening ratios are in the range $1 \lesssim R_V \lesssim 3.5$. Owing to the low sensitivity of our spectra to the Na I D absorption diagnostic (Sect. 3.1) it appears likely that we could underestimate the host extinction for some of the SNe in our sample, and the distribution of peak absolute magnitudes is systematically brighter than reported. As indicated by the small spread (a few tenths of a magnitude around light-curve peak epoch) in the colour evolution displayed in Fig. 14, in practice it seems unlikely that we have large extinction correction errors.

A 5 $\mathrm{km\,s^{-1}\,Mpc^{-1}}$ uncertainty in H_0 corresponds to an uncertainty in the distance moduli of 0.15 mag. This is a systematic error, applying equally to all SNe in the sample, and thus introduces a random uncertainty in the derived luminosity function.

Concerning the selection of the sample, the $+40$ d (after discovery) lower limit for having detections (Sect. 3) affects SNe with fast declines and means that the sample is not inclusive of such events. During the course of this work, it became clear that the post-peak P60 detections initially used to make PTF09bcl a member of the sample were actually upper limits. Owing to the good coverage of the PTF09bcl rise and peak, we did keep PTF09bcl in the sample despite that.

5.3. PTF11qnf, a SN impostor?

The question of SN impostors (Van Dyk et al. 2000; Van Dyk & Matheson 2012) is important to address. Such transients are generally less luminous than SNe IIn, but can still display the multicomponent Balmer emission lines characteristic of the SNe IIn, thus mimicking some of the SN IIn behaviour and earning them the label “impostors”. No core collapse is assumed to happen in a SN impostor. The compilation by Smith et al. (2011) shows that SN impostors typically have peak magnitudes in the range $-16 < M < -10$ mag and usually have erratic light-curve shapes. Outbursts of LBV stars is one common mechanism invoked to explain SN impostors (Smith et al. 2011). The faint end of the peak absolute magnitude distribution for our sample (Fig. 6) lies at $M \approx -17$ mag, and in this respect the majority of our sample SNe would not be regarded as SN impostors. The case of PTF11qnf, with a plateau-like and erratic light curve peaking at $M \approx -17$ mag, calls for special attention as a possible SN impostor candidate. We will attempt to evaluate the nature of PTF11qnf by comparing it to other transients showing similar behaviour (Fig. 18).

An interesting comparison can be made to the transient SNHunt248, which showed a fast rise to a double-peaked maximum lasting $\gtrsim 100$ d at $M \approx -14$ mag (Mauerhan et al. 2015; Kankare et al. 2015), interpreted by those authors as the nondestructive outburst of a hypergiant star. The deepest upper limits in the photometry from the P48 suggest that the absolute magnitude of PTF11qnf was $M_R \gtrsim -15$ between -960 to -10 d and between $+260$ to $+1950$ d, relative to the first detection (JD 2,455,866.9). This is not a deep limit, and still allows for prediscovery variability such as that observed in SNHunt248 (Kankare et al. 2015), but demonstrates that the ~ 180 d plateau episode we observe in PTF11qnf was preceded and followed by fainter periods. SN 2011A (de Jaeger et al. 2015) had a SN IIn spectrum, a maximum observed luminosity in the range between those of SNe and SN impostors, and a light curve having two plateaus. de Jaeger et al. (2015) favoured a SN impostor scenario for this transient. The 2009 outburst of the transient U2773-OT (Smith et al. 2010) exhibited a light-curve plateau of $M_R \approx -12$ mag lasting ~ 120 d, as well as Hα emission with a narrow component. Smith et al. (2010) concluded that U2773-OT was a LBV in outburst, and later studies of its $\gtrsim 15$ yr light curve led Smith et al. (2016) to compare U2773-OT to the LBV star η Car. While there is a spread of ~ 4 mag in maximum brightness, the durability of the light curves of SNHunt248, SN 2011A, and U2773-OT are similar. For comparison, Fig. 18 also shows SN 2009kn (Kankare et al. 2012), a SN IIn which had a plateau-like behaviour on a time scale similar to that of PTF11qnf, but was initially more luminous and most likely was a CC SN (Kankare et al. 2012).

The single spectrum we have of PTF11qnf (Fig. 1) was taken during its initial hump and shows a flat continuum with conspicuous Hα and Hβ emission. A Gaussian fit to its Hα narrow component gives a full width at half-maximum of $\sim 400\,\mathrm{km\,s^{-1}}$. This spectrum is comparable to some of the LBV outburst spectra compiled by Smith et al. (2011), as well as to the early spectra of SN 2011A (de Jaeger et al. 2015). The Fe II lines reported by Kankare et al. (2015) for SNhunt248 were not seen in PTF11qnf, but otherwise their spectra are comparable.

The redshift of PTF11qnf is the lowest in our sample and its host (UGC 3344) is located in a group of galaxies (LDC 410; Crook et al. 2007). This makes the distance estimate based on redshift particularly uncertain. Using the Tully-Fisher method, Lagattuta et al. (2013) obtained $\mu = 32.94$ mag for the host of PTF11qnf. In Fig. 14 $E(B-V)_{\mathrm{host}} = 0.72$ mag was assumed based on Na I D absorption, but this gives a conspicuous offset in $g - i$ toward the blue, compared to all other entries in Fig. 14. The slope of the spectrum of PTF11qnf as well as the redder colours reported for SNHunt248 by Kankare et al. (2015) suggests that we overestimate the colour excess from the PTF11qnf host. Assuming instead $E(B-V)_{\mathrm{host}} = 0.4$ mag would put PTF11qnf within the $g - i$ range of the other entries in Fig. 14. Using the Tully-Fisher μ and $E(B-V)_{\mathrm{host}} = 0.4$ mag, Fig. 18 shows that PTF11qnf might be more similar in luminosity to SNHunt248, having a late-time evolution similar to the second bump of SNHunt248.

The spectroscopic and photometric similarities of PTF11qnf to a number of transients interpreted as nondestructive outbursts of giant stars points toward this transient not being a SN, but rather an impostor. This is why we removed PTF11qnf from the analysis in Sects. 4.3 and 4.4.

5.4. Bumpy SN IIn light curves

The light curves of some SNe IIn have breaks in their post-peak decline, when the SNe temporarily rebrightens before the decline in brightness resumes. Such episodes appear as a bump in the light curve and have been seen in, for example, SNe IIn 2006jd (Stritzinger et al. 2012), 2009ip (Graham et al. 2014; Martin et al. 2015), and iPTF13z (Nyholm et al. 2017). As most SNe IIn display a mainly monotonic decline, seeing conspicuous bumps in SN IIn light curves is comparatively rare. The bumps have been proposed (e.g., Graham et al. 2014; Nyholm et al. 2017) to happen when SN ejecta encounter a region of increased density in the CSM.

Figure 2 indicates that some SNe in our sample have light-curve bumps. Photometry of the PTF10tel bump was presented by Ofek et al. (2013) while some of the other bumps have not been discussed before. The possible bump of PTF10weh (~ 0.2 mag break in the r-band decline, ~ 116 d after peak) seems to occur also in the Bgi bands, while the start of the possible bump of iPTF13aki (~ 0.4 mag rise in the r-band, 120 d after peak) is possibly also captured in the i-band. Whereas the PTF10weh bump could be a true, (pseudo)bolometric bump, the nature of the possible iPTF13aki bump is harder to evaluate. The difficulty in judging the nature of light-curve bumps is illustrated by the light curve of PTF11fzz.

For PTF11fzz, the quite conspicuous bump (~ 0.5 mag amplitude) seen around 197 d after peak is likely a consequence of the Hα line centre being shifted to 7097 Å at the redshift of PTF11fzz ($z = 0.081$). This puts the Hα emission inside the Mould R filter, but outside the SDSS r filter. We lack spectra of PTF11fzz around this epoch, but a comparison to PTF12glz (at the similar $z = 0.079$) is instructive. A large offset ($R_{\mathrm{Mould}} - r_{\mathrm{SDSS}} \approx -0.8$ mag) can be seen (Fig. 2) in our R/r photometry of PTF12glz around 220 d after its estimated peak epoch. We have a spectrum of PTF12glz taken about 235 d after its estimated peak epoch (the JD 2,456,422 Keck-I/LRIS spectrum from Soumagnac et al. 2019), which is comparable to the epoch where we see the apparent bump in PTF11fzz. Synthetic photometry on this PTF12glz spectrum using `synphot` by Ofek (2014) gives a $R_{\mathrm{Mould}} - r_{\mathrm{SDSS}} \approx -0.6$ mag difference. This is comparable to the offset we see in the observed photometry. The large offsets ($R_{\mathrm{Mould}} - r_{\mathrm{SDSS}}$) seen in two different SNe IIn both at $z \approx 0.08$, and confirmed via synthetic photometry for one of them (PTF12glz), makes it likely that the “bump” we see in PTF11fzz is a photometric filter effect.

While Ofek et al. (2013) already presented R-band photometry for PTF10tel, we have additional colour information. The precursor activity as well as the bump of both PTF10tel (~ 40 d past peak) and SN 2009ip ($\sim\ 40$ d past peak of the 2012B event) has been noted before (Ofek et al. 2013; Graham et al. 2014; Smith et al. 2014). Adding to this, in the data release by Hicken et al. (2017) we see that the Type IIn SN 2008aj has a post-peak decline and a bump comparable to bumps seen in PTF10tel and SN 2009ip. Pastorello et al. (2018) point out the similarity between SN 2009ip and a number of events with similar rise and decline rates, as well as comparable peak brightness. Here, we add SN 2008aj to that comparison and emphasise the presence of light-curve bumps.

For all three SNe, we plot the r-band light curves and the $r - i$ colour in Fig. 19. A common property of all three compared bumps is that their rises last ~ 10 d and the height of the rise is $\sim\ 0.3$ mag. We also note that the r-band decline rates pre-peak and post-peak are comparable. In $r - i$ colour, SNe 2008aj and 2009ip display a somewhat more similar behaviour pre-peak compared to PTF10tel, but all three SNe show a general progression to redder colour before the bump start. This progression slows down around the start of the bump, to resume afterwards. For comparison, the $r - i$ colour of the most durable bump of iPTF13z (called B_3 by Nyholm et al. 2017) showed a reddening before the bump, but turned bluer as the bump ended. As in iPTF13z, the bumps shown in Fig. 19 all appear in multiple optical bands, suggesting that they are driven by the continuum of the SNe rather than by (for example) Hα evolution (as in the bump of SN 2006jd; see Stritzinger et al. 2012). For SN 2009ip, an LBV star has been proposed as the progenitor (e.g. Mauerhan et al. 2013b; Smith 2017). The remarkable similarity between the evolution of SN 2008aj, SN 2009ip and PTF10tel around main peak as shown in Fig. 19 might indicate similar progenitor systems (i.e. LBV stars) for all three events.

5.5. The frequency of SN IIn light-curve bumps

Bumps in SN IIn light curves are apparently rare. Conspicuous light-curve bumps have been observed in $\lesssim 10$ SNe IIn, i.e., in $\lesssim 2\%$ of the $\gtrsim 500$ public SNe IIn listed in The Open Supernova Catalog (OSC; Guillochon et al. 2017) as of 2019 June. We will use our observations of SNe IIn from PTF/iPTF and MC simulations of detection probability to constrain the frequency of SNe IIn bumps.

The bumps are intrinsically dissimilar, in terms of amplitudes, durations, shapes, and time of occurrence in the light curve. For simplicity, we consider bump B_1 of iPTF13z (Nyholm et al. 2017) to be our model bump. Fitting a second-degree polynomial to the R-band photometry of iPTF13z between 125 and 162 rest-frame days after discovery gives $m(t) = 0.0016(t - t_0)^2 - 0.51 + \Delta m$ mag (valid within 0.51 mag of bump peak) as a simple model of bump B_1. We draw a magnitude offset Δm uniformly between 1 and 3 mag fainter than the SN peak and a time offset uniformly between 50 and 200 d after SN peak for the bump to start. This random offset relative to the peak apparent magnitude of a SN in our sample will introduce our model bump in that SN in a way resembling how the bump appeared in iPTF13z. We use the SN peak apparent magnitudes, but do not take any other light-curve property of the sample SNe into account.

To represent how SN IIn photometry is obtained, for each SN in our sample we consider all epochs when the SN was observed (after discovery) with the P48 and P60 in the photometric bands listed in Table 5. Such sets of epochs are representative for how PTF/iPTF operated, also capturing interruptions caused by e.g. cloudy nights or solar conjunction gaps. When the model bump has been introduced at a random place relative to the peak of a sample SN, the bump (stretched in time to the observer's frame) is sampled using the photometric epochs for that SN. The bump is considered to be detected if the following criteria are fulfilled: ≥ 3 epochs fall on the bump, with a time of ≥ 10 d separating the first and the last such epoch, and the faintest of the epochs giving $m \leq 20.5$ mag.

Introducing 100 such model bumps randomly (as described above) in each of the 39 SNe of our sample with measured peak epoch (Table 5) gives an acceptance fraction of $\sim 8.5\%$, i.e., the bump being detected in $\sim\ 8.5\%$ of the cases. From our observations, we know that no bump like B_1 of iPTF13z was seen in these 39 SNe in the sample. A smaller bump in PTF10tel was indeed seen, but in this MC experiment we consider only our model bump from iPTF13z. Knowing that 1 bump (B_1 itself) was detected among the 69 remaining SNe IIn from PTF/iPTF ($\sim 1.5\%$; see Table 1) allows us to make a quantitive estimate of how frequent light-curve bumps are.

We model the observation as independent observations of $N_{\rm a} = 39$ SNe IIn, calling this sample "a," with a probability $p_{\rm a} \cdot \alpha$ for a bump to be detected in one SN IIn. Here, α is the probability of SNe to feature a bump, and $p_{\rm a} = 8.5\%$ is the probability for this bump to be detected. In addition to this sample, we have sample "b," with $N_{\rm b} = 69$ SNe IIn with a bump probability $p_{\rm b} \cdot \alpha$. For this sample, we do not know the bump detection probability, and conservatively allow it to take any value between 0 and 1[4]. We model the observations as two independent samplings of SNe with a different probability to detect a bump, disregarding possible correlations due to selecting the samples. The total likelihood for the observation of $n_{\rm a} = 0$ and $n_{\rm b} = 1$ in the two samples may be written as the product of two binomial distributions, with α and $p_{\rm b}$ as parameters:

$$L(\alpha, p_{\rm b}) = Bin(n_{\rm a}|N_{\rm a}, p_{\rm a} \cdot \alpha) \cdot Bin(n_{\rm b}|N_{\rm b}, p_{\rm b} \cdot \alpha). \quad (3)$$

The maximum likelihood estimate of α is 0.014. Using the profile likelihood ratio and the assumption of an asymptotically distributed test statistic (Wilks' theorem), the 1σ confidence interval for α is $[0.0043, 0.16]$. A closer examination of the likelihood surface showed that the upper constraint on α is dominated by the term due to sample "a," while the lower edge is set by the observation of one bump in sample "b." Improved knowledge of $p_{\rm b}$ may improve the lower constraint. With the current unconstrained probability, the profiled likelihood raises $p_{\rm b}$ to 1 for low α.

From our 39 sample SNe IIn considered here and our MC experiment, we therefor estimate that bumps like the B_1 bump of iPTF13z happen in approximately $1.4^{+14.6}_{-1.0}\%$ of all SNe IIn. This interval, for our specific case of B_1, is also consistent with our rough initial estimate based on SN IIn bumps in the literature and the number of SNe IIn from the OSC.

Given the assumption that SN IIn light-curve bumps are caused by SN ejecta encountering denser regions of CSM, the rarity of such bumps is noteworthy. Modelling (e.g., Kochanek 2009) and observations (Sana et al. 2012; Dunstall et al. 2015; Kochanek 2018) suggest that at least 50% of massive stars reside in binary or multiple systems. In such binaries, the mass lost by the constituent stars can be shaped into spiral patterns

---

[4] Constraining $p_{\rm b} < p_{\rm a}$, which could be a reasonable assumption as this sample is sampled less, will move the lower edge of our confidence level up slightly.

(Tuthill et al. 2008) which could cause light-curve bumps if one of the stars explodes as a CSI-dominated SN (as invoked by Schwarz & Pringle 1996, for SN 1979C). The LBV stars, often proposed as SN IIn progenitors, are known to have structured CSM (e.g., Weis 2011) which could also lead to bumpy light curves if swept up by SN ejecta. Selection effects due to geometry and viewing angle might be at work, preventing light-curve bumps from occurring or being seen in the majority of SNe IIn. Distinctly nonspherical geometries have been demonstrated using spectropolarimetry for SNe IIn 1997eg (Hoffman et al. 2008), 1998S (Leonard et al. 2000), 2009ip (Reilly et al. 2017), and 2010jl (Patat et al. 2011). The relative rarity of light-curve bumps might be a separate indicator of nonspherical geometries in SNe IIn, or that CSM density changes big enough to cause conspicuous bumps somehow are hard to make.

A simpler explanation might be the bias caused by the short ($\gtrsim 100\,\mathrm{d}$) time window after the SN explosion during which we can discover the bumps. For typical CSM and SN ejecta velocities, a SN progenitor outburst must occur shortly before the SN in order to produce a suitably located density change causing a bump we can actually observe.

5.6. SNe IIn with plateaus and slow declines

Plateaus have been seen in the light curves of some SNe IIn, earning them the designation Type IIn-P (where "P stands for plateau). Examples are SNe 1994W (Sollerman et al. 1998), 2009kn (Kankare et al. 2012) and 2011ht (Fraser et al. 2013; Mauerhan et al. 2013a), which all exhibited plateau-like maxima lasting $\sim$ 100 days followed by a rapid decline ($\sim 0.25\,\mathrm{mag\,d^{-1}}$) from the plateau. Different models have been proposed to explain the Type IIn-P SNe, e.g. colliding CSM shells (see Dessart et al. 2016, and references therein).

In our sample, we see a version of the SNe IIn-P with a behaviour different from the examples above. Instead of dropping quickly in brightness after the plateau, the SNe we discuss instead showed a slower, linear decline after their plateaus. Among our sample SNe, we see that PTF11oxu and PTF11rfr have a rather fast rise to the plateau (rise time to plateau start $\lesssim 25\,\mathrm{d}$) and a plateau lasting $\gtrsim 50\,\mathrm{d}$, followed by a linear decline. The plateaus occur at $M_r \approx -19\,\mathrm{mag}$ and $M_r \approx -19.6\,\mathrm{mag}$ for PTF11oxu and PTF11rfr, respectively. The spectral sequence of PTF11rfr opens a possibility that the narrow component of its Hα line used to classify it as a SN Type IIn might come from the host galaxy. However, the plateau magnitude of $M_R \approx -19.6$ mag for PTF11rfr is significantly more luminous than the average SN Type IIP peak magnitude of $M_B \approx -16.80 \pm 0.37$ mag found by Richardson et al. (2014).

Vetting the literature, we find that photometry of SNe 1994Y (Ho et al. 2001) and 2005db (Kiewe et al. 2012) show comparable, but intrinsically fainter, r/R-band light curves. These light curves are plotted in Fig. 20. The I-band light curve of Type IIn SN OGLE 2013-SN-016 (Wyrzykowski et al. 2013; Nicholl et al. 2013, raw photometry by the Optical Gravitational Lensing Experiment, OGLE) also had a similar plateau duration and form. Figure 20 shows that the spread in plateau absolute magnitude is $\gtrsim$ 2 mag and that the decline rates differ after the end of the plateau. The models by van Marle et al. (2010) of SNe IIn, where the SN ejecta collide with a CSM shell, can produce light curves with plateaus of approximately the right duration and luminosity; see van Marle et al. (2010, their Figs. 11 and 12). As an example, in Fig. 20 we plot model A01 by van Marle et al. (2010), where SN ejecta hits a 6 $\mathrm{M_\odot}$ CSM shell. The steep rise and the duration of the model A01 plateau, as well as the plateau luminosity of this model, is comparable to the SNe shown. However, model A01 (and the other van Marle et al. 2010 models) gives a too steep decline after the plateau comparable to the SNe of the proposed sub-type. The slow decline of the SNe IIn here could be due to an extended CSM outside the shell. While Type IIn-P (like SN 1994W, with fast decline) have been studied by several authors, the SNe IIn with plateaus and slow declines warrants further investigation to determine if they constitute a distinct sub-type of SNe IIn.

6. Conclusions and future work

We have studied a sample of 42 SNe IIn from the untargeted PTF/iPTF survey and our main conclusions are summarised below.

- The luminosity function of SNe IIn, after compensating for Malmquist bias and K-corrections, is $M_{\mathrm{peak}} = -18.72 \pm 1.32\,\mathrm{mag}$ (if applying the $M > -21\,\mathrm{mag}$ cut to exclude ostensibly "superluminous" SNe) or $M_{\mathrm{peak}} = -19.18 \pm 1.32\,\mathrm{mag}$ (if that cut is not applied, and all SNe with Type IIn spectral signatures are included).
- The typical rise times to peak for SNe IIn are $20 \pm 8\,\mathrm{d}$ and $50 \pm 15\,\mathrm{d}$, dividing the SNe IIn into fast and slow risers.
- The typical decline rates of SNe IIn for the initial 50 d after light-curve peak can be described with the Gaussian distribution $0.012 \pm 0.008\,\mathrm{mag\,d^{-1}}$. A bimodal distribution possibly exists, with slower and faster declines (with slopes $0.013 \pm 0.008\,\mathrm{mag\,d^{-1}}$ and $0.040 \pm 0.014\,\mathrm{mag\,d^{-1}}$).
- We find no strong correlation between the peak luminosity of SNe IIn and their rise times. A correlation between the peak luminosity and the duration with ± 1 mag of peak was found, and a "Phillips-like" relation between peak absolute magnitude and decline rate can also be discerned.
- The colour evolution of SNe IIn is rather uniform. The $g - r$ colour index at peak of the sample SNe IIn is $g - r = 0.06 \pm 0.21$ mag and $g - i = 0.13 \pm 0.46$ mag.
- The SNe in the sample were hosted by galaxies of absolute magnitude $-22 \lesssim M_g \lesssim -13\,\mathrm{mag}$, i.e., with global metallicities ranging from supersolar to subsolar. No correlations between host global metallicity and SN IIn rise times, decline rates, or peak absolute magnitude were found.
- We suggest a possible new variety of "SNe IIn-P," with a light curve showing a quick rise to a $\gtrsim 50\,\mathrm{d}$ plateau, followed by a slow, linear decline. Example events include PTF11oxu and PTF11rfr, as well as SNe 1994Y and 2005db. They are thus unlike the prototypical SNe IIn-P events such as SNe 1994W and 2009kn, which dropped much faster from their plateaus.
- Light-curve bumps like the $\mathrm{B_1}$ bump of iPTF13z are rare, and happen in an estimated $1.4^{+14.6}_{-1.0}\%$ of the SNe IIn.
- K-corrections for SNe IIn at light-curve peak are found to be within 0.2 mag for the observer's frame r-band, for SNe IIn at $z < 0.25$.

The new astronomical surveys planned, or already in operation, will provide photometry of SNe IIn allowing further tests of the light curve property correlations found or rejected in this study. The new surveys will also allow more precursor outbursts (Ofek et al. 2014c; Bilinski et al. 2015) to be discovered, opening new windows to the last years of the SNe IIn progenitor stars. The Zwicky Transient Facility (ZTF, e.g. Bellm et al. 2019; Graham et al. 2019) operates an untargeted search for transients since 2018 on the P48 telescope, with a CCD camera having a field-of-view $\approx 6\times$ larger than iPTF had. During 2018 May - 2019 May, over 30 SNe IIn (spectroscopically classified) have been found by ZTF, and we could expect ZTF to produce a sample with useful rise and decline coverage for $\gtrsim$ 100 SNe IIn during the expected 3 years of survey operation. Among space based instruments, the cadence and limiting magnitude of the photometry from the Transiting Exoplanet Survey Satellite (TESS) has already proven to be useful for studies of SNe Ia (Fausnaugh et al. 2019), providing exquisite photometric coverage promising also for SNe IIn studies. In the 2020s, the Large Synoptic Survey Telescope (LSST, LSST Science Collaboration et al. 2009) will be able to provide a considerably larger sample of SN IIn light curves than previous surveys, although the cadence(s) eventually used by LSST will determine how useful the light curves will be (LSST Science Collaboration 2017). For the estimated order of $\sim 10^5$ SNe II LSST could find each year (LSST Science Collaboration et al. 2009) in its magnitude-limited survey, about $1/3$ can be expected to be SNe IIn (Li et al. 2011), giving an order of $\sim 10^4$ SN IIn candidates per year. While only a small subset of the SNe IIn found by LSST will be realistic to classify spectroscopically, the study of this diverse SN type will be drastically transformed by the copious yield of observed events.

Acknowledgements. A.N. gratefully acknowledges a grant from Stiftelsen Gustaf och Ellen Kobbs stipendiefond, and wishes to thank Ashley Villar for providing MOSFiT contours in table format for Fig. 17, Axel Runnholm for help with Python, and Maayane Soumagnac and Peter Lundqvist for discussions.

We gratefully acknowledge support from the Knut and Alice Wallenberg Foundation. The Oskar Klein Centre is funded by the Swedish Research Council. The intermediate Palomar Transient Factory project is a scientific collaboration among the California Institute of Technology, Los Alamos National Laboratory, the University of Wisconsin (Milwaukee), the Oskar Klein Centre, the Weizmann Institute of Science, the TANGO Program of the University System of Taiwan, and the Kavli Institute for the Physics and Mathematics of the Universe. This work was supported by the GROWTH project funded by the National Science Foundation under Grant No 1545949. A.V.F. is grateful for financial assistance from National Science Foundation (NSF) grant AST-1211916, the TABASGO Foundation, the Christopher R. Redlich Fund, and the Miller Institute for Basic Research in Science (U.C. Berkeley). E.O.O. is grateful for support by grants from the Israeli Ministry of Science, ISF, Minerva, BSF, BSF transformative program, Weizmann-UK, and the I-CORE Program of the Planning and Budgeting Committee and the Israel Science Foundation (grant No. 1829/12). G.L. was supported by research grant 19054 from VILLUM FONDEN. Part of this research was carried out at the Jet Propulsion Laboratory, California Institute of Technology, under a contract with the National Aeronautics and Space Administration (NASA). Based in part on observations obtained at the Gemini Observatory, under programs: GN-2010B-Q13 and GN-2010A-Q20 (PI: Howell), which is operated by the Association of Universities for Research in Astronomy, Inc., under a cooperative agreement with the NSF on behalf of the Gemini partnership: the NSF (United States), National Research Council (Canada), CONICYT (Chile), Ministerio de Ciencia, Tecnología e Innovación Productiva (Argentina), Ministério da Ciência, Tecnologia e Inovação (Brazil), and Korea Astronomy and Space Science Institute (Republic of Korea). Partly based on observations obtained with the Apache Point Observatory 3.5-m telescope, which is owned and operated by the Astrophysical Research Consortium. Some of the data presented herein were obtained at the W. M. Keck Observatory, which is operated as a scientific partnership among the California Institute of Technology, the University of California, and NASA. The Observatory was made possible by the generous financial support of the W. M. Keck Foundation. The authors wish to recognise and acknowledge the very significant cultural role and reverence that the summit of Maunakea has always had within the indigenous Hawaiian community. We are most fortunate to have the opportunity to conduct observations from this mountain. Partly based on observations at Kitt Peak National Observatory, National Optical Astronomy Observatory, which is operated by the Association of Universities for Research in Astronomy (AURA) under cooperative agreement with the NSF. The authors are honoured to be permitted to conduct astronomical research on Iolkam Du'ag (Kitt Peak), a mountain with particular significance to the Tohono O'odham. Partly based on observations made with the Nordic Optical Telescope, operated by the Nordic Optical Telescope Scientific Association at the Observatorio del Roque de los Muchachos, La Palma, Spain, of the Instituto de Astrofisica de Canarias. Partly based on observations made with the University of Hawaiis 2.2-m telescope, at Maunakea Observatory, Hawaii, USA. Partly based on observations made with the William Herschel Telescope operated on the island of La Palma by the Isaac Newton Group of Telescopes in the Spanish Observatorio del Roque de los Muchachos of the Instituto de Astrofísica de Canarias. Partly based on observations made with the 5-m Hale Telescope (P200), at Palomar Observatory, California, USA. Partly based on observations made with the Kast spectrograph on the Shane 3-m telescope at Lick Observatory, Mount Hamilton, California, USA. Research at Lick Observatory is partially supported by a generous gift from Google. We thank S. Bradley Cenko, Kelsey I. Clubb, Melissa L. Graham, Michael T. Kandrashoff, Patrick L. Kelly, Alekzandir Morton, Peter E. Nugent, and Jeffrey M. Silverman for help with some of the observations and reductions. This research used the Latest Supernovae web page (maintained by D. Bishop) and the Open Supernova Catalog (maintained by J. Guillochon and J. Parrent). This research used the SIMBAD and VizieR databases operated at CDS, Strasbourg, France, as well as the NASA/IPAC Extragalactic Database (NED) which is operated by the Jet Propulsion Laboratory, California Institute of Technology, under contract with NASA, and NASAs Astrophysics Data System. STSDAS and PyRAF are products of the Space Telescope Science Institute, which is operated by AURA for NASA. We acknowledge the whole PTF and iPTF collaborations for finding and following the SNe IIn studied in this sample.

References

Ackermann, M., Arcavi, I., Baldini, L., et al. 2015, ApJ, 807, 169
Anderson, J. P., & Soto, M. 2013, A&A, 550, A69
Anderson, J. P., James, P. A., Habergham, S. M., Galbany, L., & Kuncarayakti, H. 2015, PASA, 32, e019
Arbour, R. 2015, Central Bureau Electronic Telegrams, 4171
Aretxaga, I., Benetti, S., Terlevich, R. J., et al. 1999, MNRAS, 309, 343
Arcavi, I., Gal-Yam, A., Ofek, E., et al. 2013, The Astronomer's Telegram, 5407
Arcavi, I., Horesh, A., Sesar, B., et al. 2010, The Astronomer's Telegram, 3095
Arcavi, I., Gal-Yam, A., Kasliwal, M. M., et al. 2010, ApJ, 721, 777
Arnouts, S., Cristiani, S., Moscardini, L., et al. 1999, MNRAS, 310, 540
Bazin, G., Palanque-Delabrouille, N., Rich, J., et al. 2009, A&A, 499, 653
Bellm, E. C., Kulkarni, S. R., Graham, M. J., et al. 2019, PASP, 131, 018002
Ben-Ami, S., Badenes, C., Kulkarni, S. R., et al. 2010, The Astronomer's Telegram, 2961
Benetti, S., Cappellaro, E., Danziger, I. J., et al. 1998, MNRAS, 294, 448
Bilinski, C., Smith, N., Li, W., et al. 2015, MNRAS, 450, 246
Blagorodnova, N., Neill, J. D., Walters, R., et al. 2018, PASP, 130, 035003
Blondin, S., & Tonry, J. L. 2007, ApJ, 666, 1024
Cardelli, J. A., Clayton, G. C., & Mathis, J. S. 1989, ApJ, 345, 245
Di Carlo, E., Massi, F., Valentini, G., et al. 2002, ApJ, 573, 144
Challis, P., Foley, R. J., & Berlind, P. 2010, Central Bureau Electronic Telegrams, 2243, 1
Chevalier, R. A., & Fransson, C. 1994, ApJ, 420, 268
Cao, Y., Nugent, P. E., & Kasliwal, M. M. 2016, PASP, 128, 114502
Cenko, S. B., Fox, D. B., Moon, D.-S., et al. 2006, PASP, 118, 1396
Chatzopoulos, E., Wheeler, J. C., & Vinko, J. 2012, ApJ, 746, 121
Chilingarian, I. V., Melchior, A.-L., & Zolotukhin, I. Y. 2010, MNRAS, 405, 1409
Cikota, A., Deustua, S., & Marleau, F. 2016, ApJ, 819, 152
Cowen, D. F., Franckowiak, A., & Kowalski, M. 2010, Astroparticle Physics, 33, 19
Crook, A. C., Huchra, J. P., Martimbeau, N., et al. 2007, ApJ, 655, 790
de Boor, C. 2001, A practical guide to splines, New York: Springer, 2001
Davis, T. M., Mörtsell, E., Sollerman, J., et al. 2007, ApJ, 666, 716
Drake, A. J., Djorgovski, S. G., Graham, M. J., et al. 2011, Central Bureau Electronic Telegrams, 2948, 1
Drake, A. J., Djorgovski, S. G., Mahabal, A. A., et al. 2010, The Astronomer's Telegram, 2555
Dessart, L., Hillier, D. J., Gezari, S., Basa, S., & Matheson, T. 2009, MNRAS, 394, 21
Dessart, L., Hillier, D. J., Audit, E., Livne, E., & Waldman, R. 2016, MNRAS, 458, 2094
de la Rosa, J., Roming, P., Pritchard, T., & Fryer, C. 2016, ApJ, 820, 74
Dunstall, P. R., Dufton, P. L., Sana, H., et al. 2015, A&A, 580, A93
Duszanowicz, G. 2010, Central Bureau Electronic Telegrams, 2241, 1
Faran, T., Taubenberger, S., Kromer, M., et al. 2016, The Astronomer's Telegram, 8701
Fassia, A., Meikle, W. P. S., Vacca, W. D., et al. 2000, MNRAS, 318, 1093
Fassia, A., Meikle, W. P. S., Chugai, N., et al. 2001, MNRAS, 325, 907
Fausnaugh, M. M., Vallely, P. J., Kochanek, C. S., et al. 2019, arXiv:1904.02171
Filippenko, A. V. 1989, AJ, 97, 726
Filippenko, A. V. 1997, ARA&A, 35, 309
Flesch, E. W. 2015, PASA, 32, e010.

Fox, O. D., Filippenko, A. V., Skrutskie, M. F., et al. 2013, AJ, 146, 2
Fraser, M., Magee, M., Kotak, R., et al. 2013, ApJ, 779, L8
Fransson, C., Chevalier, R. A., Filippenko, A. V., et al. 2002, ApJ, 572, 350
Fransson, C., Ergon, M., Challis, P. J., et al. 2014, ApJ, 797, 118
Fremling, C., Sollerman, J., Taddia, F., et al. 2016, A&A, 593, A68
Fukugita, M., Ichikawa, T., Gunn, J. E., et al. 1996, AJ, 111, 1748
Galbany, L., Anderson, J. P., Sánchez, S. F., et al. 2018, ApJ, 855, 107
Gal-Yam, A., Cenko, S. B., Fox, D. B., et al. 2007a, The Multicolored Landscape of Compact Objects and Their Explosive Origins, 924, 297
Gal-Yam, A. 2012, Science, 337, 927
Gal-Yam, A., Ben-Ami, S., Arcavi, I., et al. 2012, The Astronomer's Telegram, 4293
Gal-Yam, A. 2018, arXiv e-prints , arXiv:1812.01428v1
Ganot, N., Gal-Yam, A., Ofek, E. O., et al. 2016, ApJ, 820, 57
Graham, M. L., Sand, D. J., Valenti, S., et al. 2014, ApJ, 787, 163
Graham, M. J., Kulkarni, S. R., Bellm, E. C., et al. 2019, PASP, 131, 078001
Guillochon, J., Parrent, J., Kelley, L. Z., & Margutti, R. 2017, ApJ, 835, 64
Guillochon, J., Nicholl, M., Villar, V. A., et al. 2018, ApJS, 236, 6
González-Gaitán, S., Tominaga, N., Molina, J., et al. 2015, MNRAS, 451, 2212
Habergham, S. M., Anderson, J. P., James, P. A., & Lyman, J. D. 2014, MNRAS, 441, 2230
Harutyunyan, A. H., Pfahler, P., Pastorello, A., et al. 2008, A&A, 488, 383
Hamuy, M., Phillips, M. M., Suntzeff, N. B., et al. 2003, Nature, 424, 651
Hamuy, M. 2003, ApJ, 582, 905
Hicken, M., Friedman, A. S., Blondin, S., et al. 2017, ApJS, 233, 6
Hinshaw, G., Larson, D., Komatsu, E., et al. 2013, ApJS, 208, 19
Hoffman, J. L., Leonard, D. C., Chornock, R., et al. 2008, ApJ, 688, 1186
Howell, D. A., Sullivan, M., Perrett, K., et al. 2005, ApJ, 634, 1190
Howell, D. A., & Murray, D. 2012, Central Bureau Electronic Telegrams, 3313, 2
Ho, W. C. G., Van Dyk, S. D., Peng, C. Y., et al. 2001, PASP, 113, 1349
Humphreys, R. M., & Davidson, K. 1994, PASP, 106, 1025
Ilbert, O., Arnouts, S., McCracken, H. J., et al. 2006, A&A, 457, 841
Inserra, C., Smartt, S. J., Gall, E. E. E., et al. 2018, MNRAS, 475, 1046
de Jaeger, T., Anderson, J. P., Pignata, G., et al. 2015, ApJ, 807, 63
Kankare, E., Ergon, M., Bufano, F., et al. 2012, MNRAS, 424, 855
Kankare, E., Kotak, R., Pastorello, A., et al. 2015, A&A, 581, L4
Kelly, P. L., & Kirshner, R. P. 2012, ApJ, 759, 107
Khazov, D., Yaron, O., Gal-Yam, A., et al. 2016, ApJ, 818, 3
Kiewe, M., Gal-Yam, A., Arcavi, I., et al. 2012, ApJ, 744, 10
Kobulnicky, H. A., & Kewley, L. J. 2004, ApJ, 617, 240
Kochanek, C. S. 2009, ApJ, 707, 1578
Kochanek, C. S. 2018, MNRAS, 473, 1633
Kotak, R., & Vink, J. S. 2006, A&A, 460, L5
Kulkarni, S. R. 2013, The Astronomer's Telegram, 4807
Laher, R. R., Surace, J., Grillmair, C. J., et al. 2014, PASP, 126, 674
Lagattuta, D. J., Mould, J. R., Staveley-Smith, L., et al. 2013, ApJ, 771, 88
Law, N. M., Kulkarni, S. R., Dekany, R. G., et al. 2009, PASP, 121, 1395
Leloudas, G., Hsiao, E. Y., Johansson, J., et al. 2015, A&A, 574, A61
Leonard, D. C., Filippenko, A. V., Barth, A. J., & Matheson, T. 2000, ApJ, 536, 239
Leonard, D. C., Sheehan, P., McCarthy, D., et al. 2015, The Astronomer's Telegram, 7690
Li, W., Filippenko, A. V., Van Dyk, S. D., et al. 2002, PASP, 114, 403
Li, W., Leaman, J., Chornock, R., et al. 2011, MNRAS, 412, 1441
Liddle, A. R. 2004, MNRAS, 351, L49
Liu, Q.-Z., Hu, J.-Y., Hang, H.-R., et al. 2000, A&AS, 144, 219
LSST Science Collaboration, Abell, P. A., Allison, J., et al. 2009, arXiv e-prints, arXiv:0912.0201
LSST Science Collaboration, Marshall, P., Anguita, T., et al. 2017, arXiv e-prints, arXiv:1708.04058
Malmquist, K. G. 1922, Meddelanden från Lunds Astronomiska Observatorium Serie I, 100, 1
Mauerhan, J. C., Smith, N., Silverman, J. M., et al. 2013a, MNRAS, 431, 2599
Mauerhan, J. C., Smith, N., Filippenko, A. V., et al. 2013b, MNRAS, 430, 1801
Mauerhan, J. C., Van Dyk, S. D., Graham, M. L., et al. 2015, MNRAS, 447, 1922
Martin, J. C., Hambsch, F.-J., Margutti, R., et al. 2015, AJ, 149, 9
van Marle, A. J., Smith, N., Owocki, S. P., & van Veelen, B. 2010, MNRAS, 407, 2305
Masci, F. J., Laher, R. R., Rebbapragada, U. D., et al. 2017, PASP, 129, 014002
Masci, F. J., Papadogiannakis, S., Laher, R. R., et al. 2015, Generating Light Curves from Forced PSF-fit Photometry on PTFIDE Difference-images
Mould, J. R., Huchra, J. P., Freedman, W. L., et al. 2000, ApJ, 529, 786
Mould, J. R., Huchra, J. P., Freedman, W. L., et al. 2000, ApJ, 545, 547
Moriya, T. J., & Maeda, K. 2014, ApJ, 790, L16
Moriya, T. J., Maeda, K., Taddia, F., et al. 2014, MNRAS, 439, 2917
Moriya, T. J., Sorokina, E. I., & Chevalier, R. A. 2018, Space Sci. Rev., 214, #59
Nadyozhin, D. K. 1994, ApJS, 92, 527
Nicholl, M., Walton, N., Blagorodnova, N., et al. 2013, The Astronomer's Telegram, 4860
Nyholm, A., Sollerman, J., Taddia, F., et al. 2017, A&A, 605, A6
Ochsenbein, F., Bauer, P., & Marcout, J. 2000, A&AS, 143, 23
Ofek, E. O., Zoglauer, A., Boggs, S. E., et al. 2014a, ApJ, 781, 42
Ofek, E. O., Arcavi, I., Tal, D., et al. 2014b, ApJ, 788, 154
Ofek, E. O., Sullivan, M., Shaviv, N. J., et al. 2014c, ApJ, 789, 104
Ofek, E. O. 2014, Astrophysics Source Code Library, ascl:1407.005
Ofek, E. O., Sullivan, M., Cenko, S. B., et al. 2013, Nature, 494, 65
Ofek, O. 2012, Central Bureau Electronic Telegrams, 3313, 1
Ofek, E. O., Laher, R., Law, N., et al. 2012, PASP, 124, 62
Ofek, E. O., Rabinak, I., Neill, J. D., et al. 2010, ApJ, 724, 1396
Papadogiannakis, S., Goobar, A., Amanullah, R., et al. 2019, MNRAS, 483, 5045
Patat, F., Taubenberger, S., Benetti, S., Pastorello, A., & Harutyunyan, A. 2011, A&A, 527, L6
Pastorello, A., Kochanek, C. S., Fraser, M., et al. 2018, MNRAS, 474, 197
Perley, D. A., Quimby, R. M., Yan, L., et al. 2016, ApJ, 830, 13
Petrosian, V. 1976, ApJ, 209, L1
Phillips, M. M. 1993, ApJ, 413, L105
Pskovskii, I. P. 1977, Soviet Ast., 21, 675
Reilly, E., Maund, J. R., Baade, D., et al. 2017, MNRAS, 470, 1491
Richardson, D., Branch, D., Casebeer, D., et al. 2002, AJ, 123, 745
Richardson, D., Jenkins, R. L., III, Wright, J., & Maddox, L. 2014, AJ, 147, 118
Roming, P. W. A., Kennedy, T. E., Mason, K. O., et al. 2005, Space Sci. Rev., 120, 95
Rubin, A., Gal-Yam, A., De Cia, A., et al. 2016, ApJ, 820, 33
Sana, H., de Mink, S. E., de Koter, A., et al. 2012, Science, 337, 444
Schlafly, E. F., & Finkbeiner, D. P. 2011, ApJ, 737, 103
Schlegel, E. M. 1990, MNRAS, 244, 269
Schwarz, D. H., & Pringle, J. E. 1996, MNRAS, 282, 1018
Silverman, J. M., Nugent, P. E., Gal-Yam, A., et al. 2013, ApJS, 207, 3
Sollerman, J., Cumming, R. J., & Lundqvist, P. 1998, ApJ, 493, 933
Sollerman, J., Mörtsell, E., Davis, T. M., et al. 2009, ApJ, 703, 1374
Soumagnac, M. T., Ofek, E. O., Gal-yam, A., et al. 2019, ApJ, 872, 141
Smith, N., Li, W., Foley, R. J., et al. 2007, ApJ, 666, 1116
Smith, N., & McCray, R. 2007, ApJ, 671, L17
Smith, N., Miller, A., Li, W., et al. 2010, AJ, 139, 1451
Smith, N., Li, W., Silverman, J. M., Ganeshalingam, M., & Filippenko, A. V. 2011, MNRAS, 415, 773
Smith, N. 2014, ARA&A, 52, 487
Smith, N., Mauerhan, J. C., & Prieto, J. L. 2014, MNRAS, 438, 1191
Smith, N. 2016, "Interacting Supernovae: Types IIn and Ibn," Handbook of Supernovae, Springer
Smith, N., Andrews, J. E., Mauerhan, J. C., et al. 2016, MNRAS, 455, 3546
Smith, N. 2017, Philosophical Transactions of the Royal Society of London Series A, 375, 20160268
Stathakis, R. A., & Sadler, E. M. 1991, MNRAS, 250, 786
Stoll, R., Prieto, J. L., Stanek, K. Z., & Pogge, R. W. 2013, ApJ, 773, 12
Stritzinger, M., Taddia, F., Fransson, C., et al. 2012, ApJ, 756, 173
Taubenberger, S., Pastorello, A., Mazzali, P. A., et al. 2006, MNRAS, 371, 1459
Taddia, F., Stritzinger, M. D., Sollerman, J., et al. 2013, A&A, 555, A10
Taddia, F., Sollerman, J., Fremling, C., et al. 2015, A&A, 580, A131
Taddia, F., Sollerman, J., Fremling, C., et al. 2019, A&A, 621, A71
Tremonti, C. A., Heckman, T. M., Kauffmann, G., et al. 2004, ApJ, 613, 898
Turatto, M., Cappellaro, E., Danziger, I. J., et al. 1993, MNRAS, 262, 128
Tuthill, P. G., Monnier, J. D., Lawrance, N., et al. 2008, ApJ, 675, 698
Valenti, S., Howell, D. A., Stritzinger, M. D., et al. 2016, MNRAS, 459, 3939
Weis, K. 2011, Active OB Stars: Structure, Evolution, Mass Loss, and Critical Limits, 272, 372
Van Dyk, S. D., Peng, C. Y., King, J. Y., et al. 2000, PASP, 112, 1532
Van Dyk, S. D., & Matheson, T. 2012, Eta Carinae and the Supernova Impostors, 384, 249
Villar, V. A., Berger, E., Metzger, B. D., & Guillochon, J. 2017, ApJ, 849, 70
Wyrzykowski, L., Udalski, A., & Kozlowski, S. 2013, The Astronomer's Telegram, 4859
Yaron, O., & Gal-Yam, A. 2012, PASP, 124, 668
Young, D. 2016, Transient Name Server Discovery Report, 61
Zhang, J., & Wang, X. 2015, The Astronomer's Telegram, 6939, 1

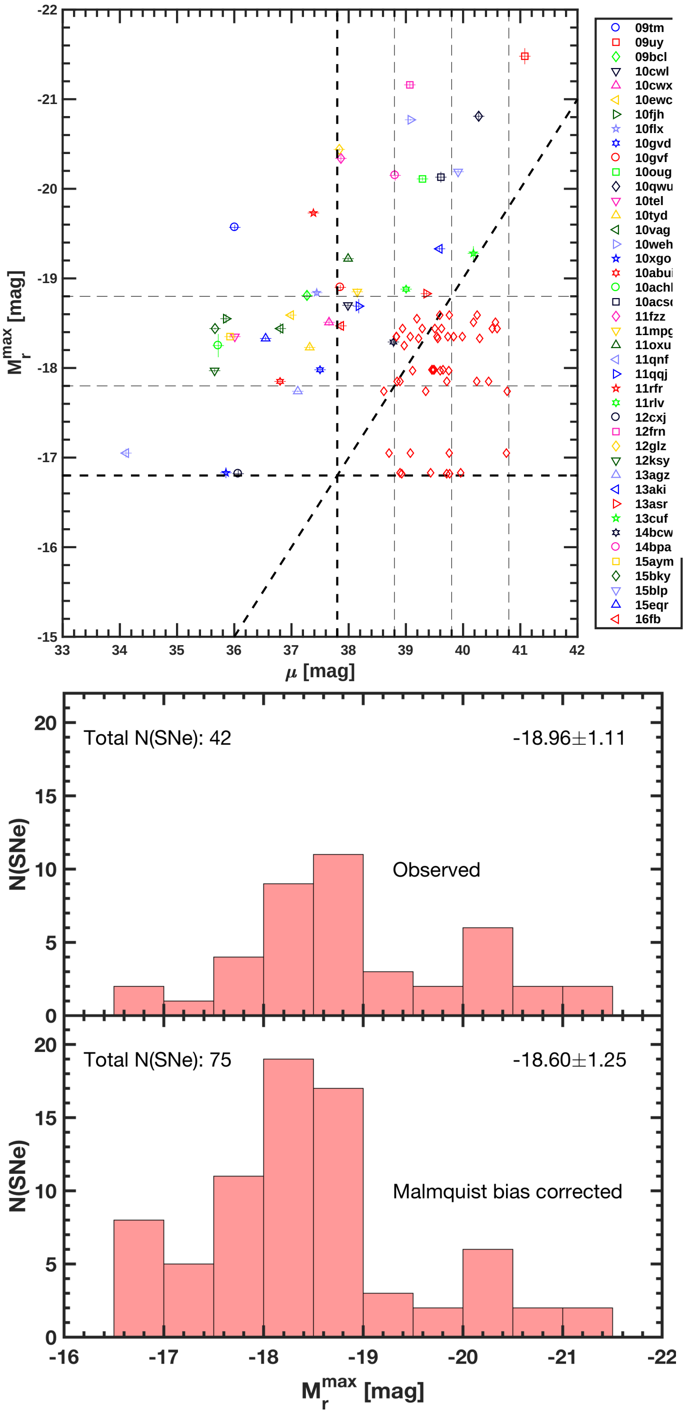

Figure 15 (Upper panel) The peak absolute magnitudes as a function of the distance moduli (μ) of the 42 SNe in the sample, shown with the randomly generated SNe IIn (empty red diamonds) introduced to compensate for Malmquist bias. The limiting magnitude $m = 21$ typical for PTF/iPTF under favourable conditions is shown as a diagonal, dashed line. (Lower panel) Histograms of the observed and bias-compensated luminosity distributions of the SNe IIn at peak brightness. Bias compensation follows Richardson et al. (2014) and Taddia et al. (2019). K-corrections are not taken into account in the results plotted here, but are studied in Sect. 4.6.

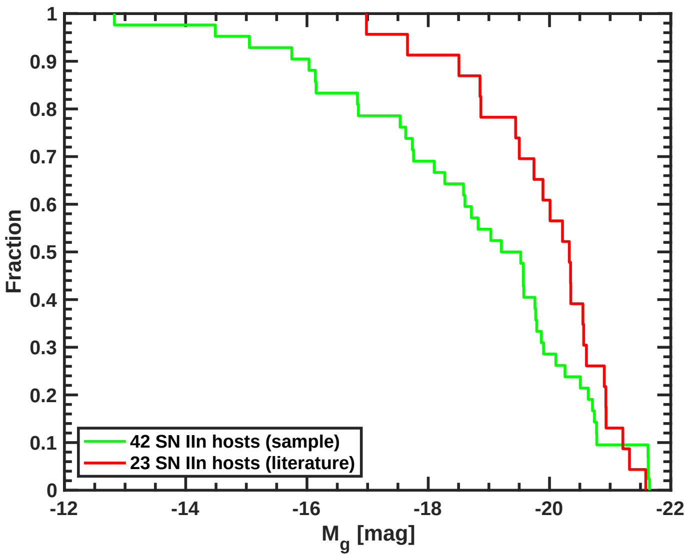

Figure 16 Cumulative distribution plot of host-galaxy SDSS/Pan-STARRS g-band absolute magnitudes (from Schulze et al., in prep.) for the 42 hosts of our sample SNe and for 23 SN IIn hosts in the SDSS field from the Taddia et al. (2015) sample.

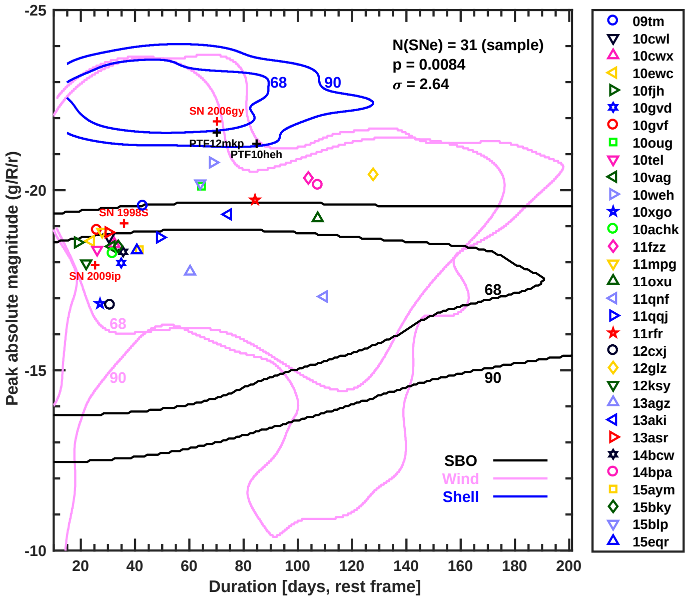

Figure 17 Percentile contours for the DLPS of CSI-driven SNe as explored by Villar et al. (2017) using the MOSFiT code (Guillochon et al. 2018). SN-like events are shown in pink (wind-like CSM) and blue (shell-like CSM) whereas shock-breakout (SBO) transients are shown in black. For each contour colour, the inner contour represents the 68th percentile and the outer contour the 90th percentile. From our sample, 31 SNe are plotted, along with the SLSNe IIn PTF10heh and PTF12mkp. For comparison, the much-studied SNe 1998S (Liu et al. 2000), 2006gy (Smith et al. 2007a), and 2009ip (2012B event, Graham et al. 2014) are included as well.

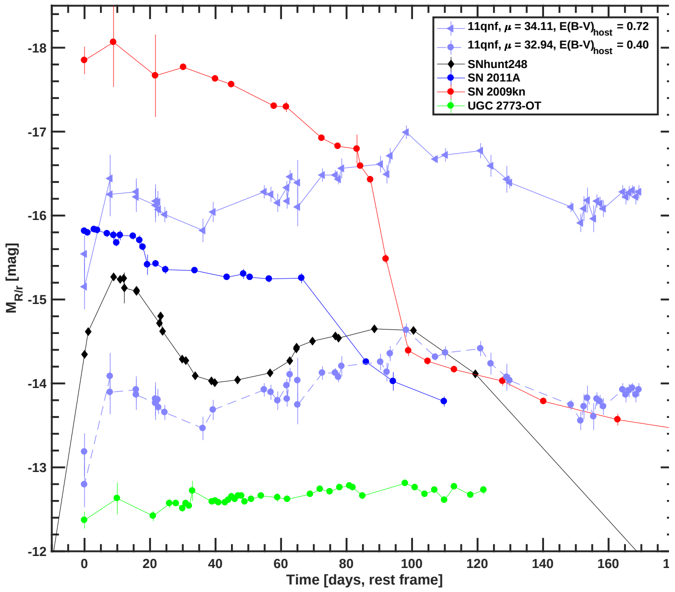

Figure 18 Comparison of R/r-band light curves PTF11qnf and SNhunt248 (Kankare et al. 2015), SN 2011 (de Jaeger et al. 2015), SN 2009kn (Kankare et al. 2012), an U2773-OT (2009 outburst; Smith et al. 2010). Distance modu and extinction values are taken from the respective works. For PTF11qnf, we show the light curve assuming $\mu = 34.11$ mag given in Table 4 and the $E(B-V)_{\rm host}$ from Sect. 3.1, as well as assuming the Tully-Fisher based $\mu = 32.94$ mag of Lagattuta et al. (2013), and the $E(B-V)_{\rm host}$ estimated in Sect. 5.3. Epoch 0 d is set at the first detection in the light curve (for PTF11qnf, SN 2009kn, and SN 2011A) or the observed start of the outburst episodes (for SNhunt248 and U2773-OT). Lines are drawn to guide the eye.

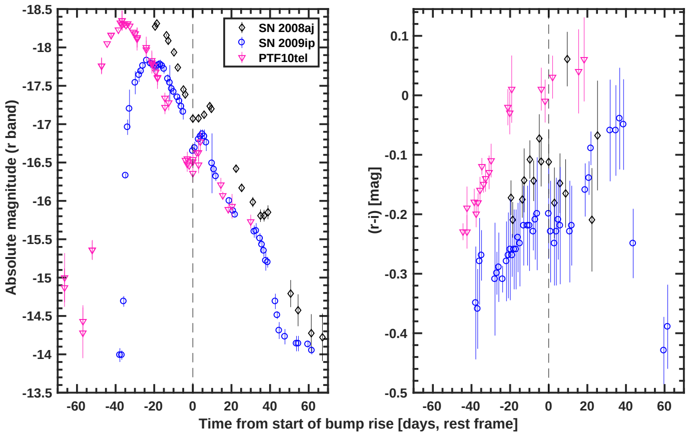

Figure 19 Comparison of the r-band magnitudes and $r-i$ colours for the bumps seen in Type IIn SNe 2008aj, 2009ip (2012B event), and PTF10tel. Photometry and extinction corrections are taken from Hicken et al. (2017), Graham et al. (2014), and this paper, respectively. For clarity, colour data points with uncertainties > 0.1 mag are not shown.

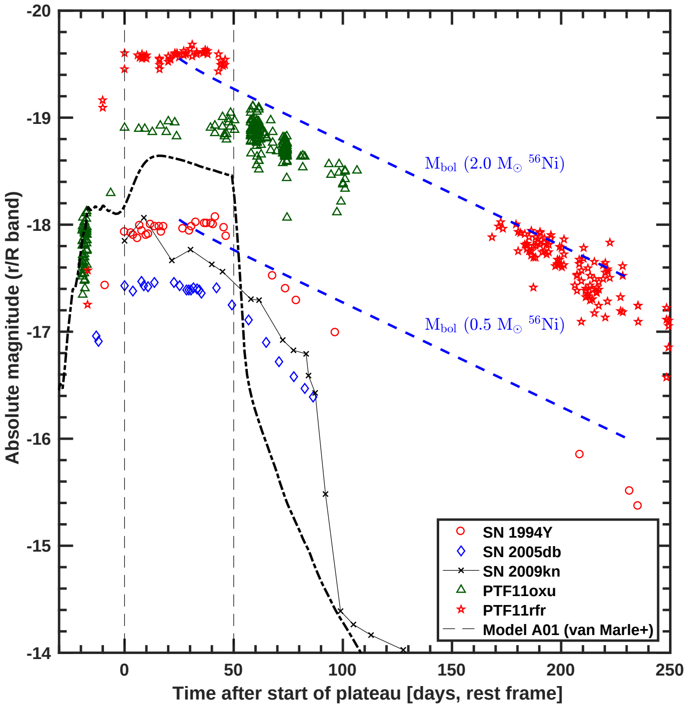

Figure 20 SNe IIn with rapid rises, plateau-like maxima, and linear declines. Shown here are SNe 1994Y (Ho et al. 2001) and 2005db (Kiewe et al. 2012), along with the sample SNe PTF11oxu and PTF11rfr. For comparison, the Type IIP-n SN 2009kn (Kankare et al. 2012) is also displayed. Dashed vertical lines highlight 50 d plateau duration. Also, the bolometric decay rates (Nadyozhin 1994) for 0.5 and 2.0 $M_\odot$ of synthesised ^{56}Ni are shown as dashed blue lines (assuming a rise time to plateau start of 20 d) for comparison. They are not fits to the photometry. Model A01 (bolometric luminosity) by van Marle et al. (2010) is also shown.

Table 1. Sample studies of SNe IIn based on optical observations

Reference	Sample size	Lowest z in sample	Median z in sample	Maximum z in sample	Mode of sample source survey(s)	Main area of study
Li et al. (2002)	7	0.0022	0.0047	0.018	Targeted	Late-time photometry
Richardson et al. (2002)	9	0.0028	0.0082	0.043	Targeted	Luminosity function
Li et al. (2011)	7	0.0024	0.0088	0.012	Targeted	Luminosity function
Kiewe et al. (2012)	4	0.015	0.024	0.031	Targeted	Light-curves and spectra
Taddia et al. (2013)	7	0.0071	0.017	0.029	Mainly targeted	Light-curves and spectra
Ofek et al. (2014b)	19	0.031	0.073	0.28	Untargeted	Rise times
Ofek et al. (2014c)	16	0.004	0.031	0.14	Mainly untargeted	Precursor outbursts
Richardson et al. (2014)	31	0.0021	0.016	0.35	Mainly targeted	Luminosity function
Bilinski et al. (2015)	6	0.0061	0.0095	0.011	Targeted	Precursor outbursts
de la Rosa et al. (2016)	8	0.004	0.01	0.017	Mainly targeted	Light-curves
This work	42	0.014	0.078	0.313	Untargeted	Light-curves

Note. — The works included in the table all discuss photometric properties of SNe IIn. For the sample size counts, the SNe labeled as SNe IIn by the respective authors were used. If available, the redshifts of the SNe in each sample were taken from the respective papers. Otherwise, distance moduli or luminosity distances given in the papers were converted to redshifts using cosmological parameters from Sect. 3 without infall correction. Li et al. (2002) gives no distance information for their sample SNe; here, NED redshifts for their respective SN host galaxies were used.

Table 2. Log of the classification spectra for the 42 SNe IIn in our sample

SN	MJD	SN age, relative to peak (days, rest frame)	Telescope	Instrument
PTF09tm	55037	8	Lick	Kast
PTF09uy	55008	-23	Keck I	LRIS
PTF09bcl	55055	9	WHT	ISIS
PTF10cwl	55270	4	Keck I	LRIS
PTF10cwx	55273	1	P200	DBSP
PTF10ewc	55285	-14	WHT	ISIS
PTF10fjh	55300	-8	Gemini N	GMOS
PTF10flx	55299	-6	Gemini N	GMOS
PTF10gvd	55322	9	Keck I	LRIS
PTF10gvf	55323	-13	Keck I	LRIS
PTF10oug	55396	-30	P200	DBSP
PTF10qwu	55421	–	P200	DBSP
PTF10tel	55434	-11	Gemini North	GMOS
PTF10tyd	55443	-23	P200	DBSP
PTF10vag	55454	-10	Lick	Kast
PTF10weh	55502	-2	Lick	Kast
PTF10xgo	55477	-2	P200	DBSP
PTF10abui	55536	-10	P200	DBSP
PTF10achk	55547	-5	UH	SNIFS
PTF10acsq	55574	–	P200	DBSP
PTF11fzz	55736	-51	P200	DBSP
PTF11mpg	55833	6	Keck II	DEIMOS
PTF11oxu	55872	-37	WHT	ISIS
PTF11qnf	55892	-76	Keck I	LRIS
PTF11qqj	55895	-7	P200	DBSP
PTF11rfr	55916	-30	P200	DBSP
PTF11rlv	55953	20	Kitt Peak	RC Spec
PTF12cxj	56035	-14	Gemini North	GMOS
PTF12frn	56124	4	Keck II	DEIMOS
PTF12glz	56123	-58	P200	DBSP
PTF12ksy	56238	-14	P200	DBSP
iPTF13agz	56442	26	Apache Point	DIS
iPTF13aki	56395	-7	P200	DBSP
iPTF13asr	56421	2	Keck I	LRIS
iPTF13cuf	56545	–	Keck II	DEIMOS
iPTF14bcw	56803	-16	Keck II	DEIMOS
iPTF14bpa	56832	-28	P200	DBSP
iPTF15aym	57176	-13	NOT	ALFOSC
iPTF15bky	57196	-8	NOT	ALFOSC
iPTF15blp	57226	17	P200	DBSP
iPTF15eqr	57362	-10	Keck I	LRIS
iPTF16fb	57445	4	P200	DBSP

Note. — The spectra were taken at epochs -11 ± 20 d (1σ Gaussian spread) relative to light-curve peak. For our spectroscopy, we used the following telescopes (with spectrographs given in parenthesis): Apache Point 3.5 m (DIS, Dual Imaging Spectrograph), Gemini North 8.1 m (GMOS, Gemini Multi-Object Spectrograph), Keck I 10 m (LRIS, Low-Resolution Imaging Spectrometer), Keck II 10 m (DEIMOS, DEep Imaging Multi-Object Spectrograph), Kitt Peak 4 m (Ritchey-Chretien Spectrograph), Lick 3 m Shane telescope (Kast Double Spectrograph), NOT 2.5 m (ALFOSC, Alhambra Faint Object Spectrograph and Camera), P200 5.1 m Hale telescope (DBSP, Double Spectrograph), University of Hawaii (UH) 2.2 m (SNIFS, Supernova Integral Field Spectrograph) & William Herschel Telescope (WHT) 4.2 m (ISIS, Intermediate-dispersion Spectrograph and Imaging System). For SNe with age ”–” when the spectrum was taken, no peak epoch was determined.

Table 3. SN IIn sample selection

Selection of SNe	Number of SNe
All SNe found and classified by PTF/iPTF 2009–2017	3018
Spectroscopically classified SNe II	692
Spectroscopically classified SNe IIn	111
SNe IIn having upper limits less than 40 d before discovery	55
SNe IIn also having detections past 40 d after discovery	42

Note. — The selection of SNe II(n) in each row is a subset of the SNe in the row above. The 692 “SNe II” include SNe IIP/L/b/n. The 40 d mentioned is in the observer’s frame. The 15 SLSNe II found by PTF/iPTF are not included in the SNe II row and below.

Table 4. The 42 SNe IIn in the sample

SN	α (J2000.0) (h:m:s)	δ (J2000.0) ($^\circ$:$'$:$''$)	Redshift (heliocentric)	μ (mag)	Discovery date (MJD)	$E(B-V)_{\mathrm{MW}}$ (mag)	M_g^{host} (mag)	Alternative designations	Discovery announcement(s)	Inclusion in other samples
PTF09tm	13:46:55.94	+61:33:15.6	0.03492	36.01	55005.31	0.016	−20.1	–	–	A10
PTF09uy	12:43:55.80	+74:41:08.1	0.31351	41.08	55005.33	0.020	−18.1	–	–	A15
PTF09bcl	18:06:26.78	+17:51:43.0	0.06205	37.27	55034.20	0.081	−21.63	–	–	A10; A15
PTF10cwl	12:36:22.06	+07:47:38.0	0.08489	37.99	55268.23	0.019	−17.74	CSS100320:123622+074737	Drake et al. (2010)	O14b; A15
PTF10cwx	12:33:16.53	−00:03:10.6	0.07312	37.66	55268.24	0.022	−18.71	–	–	A10; O14b; A15
PTF10ewc	14:01:59.08	+33:50:11.6	0.05424	36.99	55284.33	0.013	−17.76	–	–	A15
PTF10fjh	16:46:55.36	+34:09:34.7	0.03209	35.86	55296.26	0.021	−21.65	SN 2010bq	Duszanowicz (2010); Challis et al. (2010)	O14c; A15
PTF10flx	16:46:58.28	+64:26:48.5	0.06744	37.44	55297.43	0.026	−19.86	–	–	A15
PTF10gvd	16:53:02.12	+67:00:08.9	0.06928	37.50	55322.27	0.036	−16.14	–	–	A15
PTF10gvf	11:13:45.24	+53:37:44.9	0.08092	37.85	55322.22	0.010	−19.77	–	–	O14b; O14c; A15
PTF10oug	17:20:44.79	+29:04:25.6	0.15007	39.29	55391.28	0.037	−18.61	–	–	O14b; A15
PTF10qwu	16:51:10.36	+28:18:06.2	0.22585	40.27	55417.21	0.040	−16.03	–	–	A15
PTF10tel	17:21:30.68	+48:07:47.4	0.03487	36.01	55433.18	0.015	−16.83	SN 2010mc	Ofek (2012); Howell & Murray (2012)	O14b; O14c; A15
PTF10tyd	17:09:19.41	+27:49:08.6	0.06325	37.32	55440.15	0.058	−20.51	–	–	O14b; A15
PTF10vag	21:47:18.48	+18:07:51.5	0.05156	36.81	55451.16	0.106	−15.75	–	–	O14b; A15
PTF10weh	17:26:50.46	+58:51:07.4	0.13788	39.08	55461.18	0.028	−12.82	–	Ben-Ami et al. (2010)	O14b; O14c; A15
PTF10xgo	21:55:57.38	+01:19:14.1	0.03359	35.85	55472.29	0.048	−17.54	–	–	A15
PTF10abui	06:12:18.46	−22:46:15.6	0.05162	36.80	55535.29	0.062	−19.57	–	Arcavi et al. (2010)	A15
PTF10achk	03:05:57.54	−10:31:21.0	0.03248	35.72	55545.10	0.056	−20.74	–	–	O14b; O14c; A15
PTF10acsq	08:01:33.17	+46:45:52.5	0.17303	39.61	55558.36	0.063	−16.85	–	–	A15
PTF11fzz	11:10:46.68	+54:06:18.8	0.08132	37.86	55730.20	0.009	−14.49	–	–	O14b; O14c; A15
PTF11mpg	22:17:36.66	+00:36:48.4	0.09334	38.15	55824.26	0.050	−18.58	PS1-11aqj	Pan-STARRS Alerts	A15
PTF11oxu	03:38:34.38	+22:32:59.4	0.08780	37.99	55853.30	0.176	−21.62	SN 2011jc	Drake et al. (2011)	A15
PTF11qnf	05:44:54.14	+69:09:06.9	0.01481	34.11	55888.40	0.106	−20.64	–	–	A15
PTF11qqj	09:58:01.64	+00:43:14.7	0.09310	38.18	55891.44	0.025	−19.03	PS1-12y	–	A15
PTF11rfr	01:42:16.98	+29:16:25.7	0.06751	37.38	55906.08	0.042	−18.82	–	–	O14c; A15
PTF11rlv	12:49:34.04	−09:20:40.5	0.13234	39.00	55922.50	0.037	−19.79	–	–	A15
PTF12cxj	13:12:38.68	+46:29:06.3	0.03559	36.07	56033.29	0.010	−19.57	–	–	O14b; O14c; A15
PTF12frn	16:22:00.16	+32:09:38.9	0.13647	39.07	56096.43	0.019	−20.78	–	–	Ganot et al. (2016)
PTF12glz	15:54:53.04	+03:32:07.5	0.07927	37.84	56114.22	0.130	−19.76	–	Gal-Yam et al. (2012)	O14b, Ganot et al. (2016)
PTF12ksy	04:11:46.09	−12:28:00.8	0.03143	35.66	56237.29	0.037	−20.71	–	–	O14b
iPTF13agz	14:34:32.12	+25:09:43.6	0.05715	37.11	56386.36	0.028	−19.9	–	–	O14b
iPTF13aki	14:35:34.35	+38:38:31.0	0.16996	39.59	56392.25	0.010	−18.27	–	This work	–
iPTF13asr	12:47:28.61	+27:04:03.6	0.15427	39.36	56415.27	0.011	−19.57	–	This work	–
iPTF13cuf	02:04:52.97	+14:37:59.7	0.21994	40.18	56516.44	0.041	−16.15	–	Arcavi et al. (2013)	–
iPTF14bcw	13:48:41.18	+35:52:17.1	0.12058	38.78	56803.29	0.009	−15.05	–	This work	–
iPTF14bpa	15:26:59.96	+24:41:17.5	0.12197	38.81	56820.21	0.037	−20.78	PS15aod	PS1 Object List	–
iPTF15aym	13:26:26.67	+55:23:43.4	0.03344	35.93	57168.24	0.012	−19.2	–	This work	–
iPTF15bky	15:04:40.80	+12:37:43.4	0.02877	35.66	57192.35	0.032	−21.63	SN 2015Z	?Leonard et al. (2015)	–
iPTF15blp	16:27:15.21	+41:08:58.1	0.19486	39.91	57193.32	0.006	−17.63	PS15axx	PS1 Object List	–
iPTF15eqr	04:01:15.67	+33:16:58.3	0.04671	36.55	57361.22	0.354	−20.25	AT 2016oy, PS16qg	Young (2016)	–
iPTF16fb	10:22:09.25	+15:28:19.2	0.08112	37.87	57427.46	0.045	−19.52	SN 2016afj, PS16ago	Faran et al. (2016)	–

Note. — The distance modulus μ and Milky Way colour excess $E(B-V)_{\mathrm{MW}}$ for each SN is obtained as described in Sect. 3.1. The given discovery date refers to the time of PTF/iPTF discovery ($MJD = JD$-$2,400,000.5$), i.e., the epoch of the image which prompted a human scanner in the PTF/iPTF project to flag the transient as a candidate SN. The mean statistical error of the heliocentric redshifts z is $\sigma_z = 0.00025$, but the resolution of our spectra (typically a few $\times 10^2$ km s^{-1}) suggests that $\sigma_z \approx 0.001$ is a more realistic error estimate. The host galaxy g-band absolute magnitudes (M_g^{host}) were obtained as described in Sect. 4.7. The majority of SNe in our sample have been included in some (or all) of the following three earlier SN IIn samples in the literature: Ofek et al. (2014b, O14a in the table), Ofek et al. (2014c, O14b in the table), and Ackermann et al. (2015, A15 in the table). The general SN II sample by Arcavi et al. (2010, A10 in the table) and the work by Ganot et al. (2016) also included some of the SNe in our sample.

Table 5. Peak magnitudes, rise times, explosion epochs, peak epochs, and decline rates for the 42 SNe IIn in the sample

SN	Peak abs. mag $\pm1\sigma$	Peak app. mag $\pm1\sigma$	Rise time (rest frame)$\pm1\sigma$ (days)	Expl. MJD $\pm1\sigma$ (obs. frame)	Peak MJD $\pm1\sigma$ (obs. frame)	0–50 days decline $\pm1\sigma$ ($\mathrm{mag\,d^{-1}}$)	CSS spline smoothing parameter $\times100$	Band
PTF09tm	-19.57 ± 0.03	16.93 ± 0.03	23.90 ± 1.97	55003.91 ± 1.22	55028.65 ± 1.63	$--$	1.000	R/r
PTF09uy	-21.48 ± 0.09	19.65 ± 0.09	43.76 ± 15.25	54980.45 ± 19.98	55037.92 ± 1.50	0.0288 ± 0.0040	0.500	R/r
PTF09bcl	-18.81 ± 0.05	18.67 ± 0.05	12.80 ± 1.33	55031.96 ± 0.93	55045.55 ± 1.06	$--$	1.000	R
PTF10cwl	-18.70 ± 0.03	19.34 ± 0.03	12.61 ± 1.95	55251.09 ± 1.83	55264.77 ± 1.06	0.0382 ± 0.0027	0.400	R
PTF10cwx	-18.51 ± 0.04	19.20 ± 0.04	26.49 ± 2.11	55243.69 ± 1.95	55272.11 ± 1.15	0.0518 ± 0.0060	4.000	R
PTF10ewc	-18.59 ± 0.04	18.43 ± 0.04	28.08 ± 4.98	55270.45 ± 5.24	55300.06 ± 0.36	0.0400 ± 0.0018	6.000	R
PTF10fjh	-18.55 ± 0.05	17.36 ± 0.05	14.41 ± 1.13	55293.18 ± 0.89	55308.06 ± 0.76	0.0570 ± 0.0034	3.000	R/r
PTF10flx	-18.84 ± 0.04	18.66 ± 0.03	$--$	$--$	55304.92 ± 1.01	0.0362 ± 0.0018	1.000	R
PTF10gvd	-17.98 ± 0.05	19.62 ± 0.05	11.65 ± 3.47	55299.99 ± 3.22	55312.44 ± 1.85	0.0210 ± 0.0019	7.000	R
PTF10gvf	-18.90 ± 0.03	18.98 ± 0.03	14.78 ± 1.34	55320.63 ± 1.06	55336.61 ± 0.99	$--$	4.000	R
PTF10oug	-20.11 ± 0.02	19.28 ± 0.02	51.05 ± 3.95	55371.29 ± 4.33	55430.00 ± 1.39	0.0196 ± 0.0011	0.030	R
PTF10qwu	-20.81 ± 0.05	19.57 ± 0.05	$--$	$--$	$--$	$--$	4.000	R/r
PTF10tel	-18.35 ± 0.02	17.70 ± 0.02	16.28 ± 0.47	55428.22 ± 0.00	55445.07 ± 0.49	0.0422 ± 0.0015	1.000	R/r
PTF10tyd	-18.23 ± 0.03	19.23 ± 0.03	45.10 ± 4.10	55419.09 ± 3.37	55467.04 ± 2.76	$--$	0.100	R
PTF10vag	-18.44 ± 0.06	18.65 ± 0.04	17.78 ± 1.27	55445.63 ± 0.58	55464.33 ± 1.20	0.0542 ± 0.0051	2.000	R/r
PTF10weh	-20.77 ± 0.01	18.39 ± 0.01	49.27 ± 1.63	55448.58 ± 1.61	55504.64 ± 0.93	0.0148 ± 0.0003	0.100	R/r
PTF10xgo	-16.85 ± 0.06	19.14 ± 0.03	26.36 ± 2.57	55452.09 ± 2.40	55479.34 ± 1.14	0.0314 ± 0.0019	3.000	R/r
PTF10abui	-17.85 ± 0.03	19.10 ± 0.03	$--$	$--$	55546.94 ± 1.44	$--$	0.090	R
PTF10achk	-18.25 ± 0.13	17.63 ± 0.13	29.56 ± 3.94	55521.39 ± 3.07	55551.91 ± 2.67	0.0310 ± 0.0048	1.000	R/r
PTF10acsq	-20.13 ± 0.06	19.65 ± 0.06	$--$	$--$	$--$	$--$	5.000	R/r
PTF11fzz	-20.34 ± 0.04	17.55 ± 0.03	62.36 ± 3.91	55723.86 ± 1.74	55791.29 ± 3.85	0.0064 ± 0.0003	0.800	R/r
PTF11mpg	-18.85 ± 0.04	19.44 ± 0.04	15.81 ± 2.76	55809.05 ± 2.44	55826.34 ± 1.78	0.0396 ± 0.0057	8.000	R/r
PTF11oxu	-19.22 ± 0.02	19.21 ± 0.02	68.93 ± 5.48	55837.33 ± 4.16	55912.31 ± 4.26	0.0080 ± 0.0003	0.010	R
PTF11qnf	-17.05 ± 0.05	19.32 ± 0.05	134.86 ± 4.70	55831.70 ± 2.23	55968.55 ± 4.22	0.0166 ± 0.0010	4.000	R/r
PTF11qqj	-18.69 ± 0.08	19.55 ± 0.08	$--$	$--$	55903.18 ± 1.83	0.0148 ± 0.0016	0.100	R
PTF11rfr	-19.73 ± 0.01	17.76 ± 0.01	49.70 ± 2.60	55895.39 ± 0.07	55948.44 ± 2.78	0.0134 ± 0.0015	1.000	R
PTF11rlv	-18.88 ± 0.05	20.22 ± 0.05	$--$	$--$	55930.38 ± 3.02	$--$	0.006	R
PTF12cxj	-16.82 ± 0.04	19.28 ± 0.04	22.21 ± 2.00	56026.30 ± 1.95	56049.30 ± 0.70	0.0378 ± 0.0032	0.200	R
PTF12frn	-21.16 ± 0.04	19.42 ± 0.04	37.85 ± 2.82	56076.92 ± 3.00	56119.94 ± 1.12	$--$	0.500	R
PTF12glz	-20.44 ± 0.02	17.75 ± 0.01	62.75 ± 1.03	56118.16 ± 0.97	56185.88 ± 0.55	0.0052 ± 0.0001	0.002	R/r
PTF12ksy	-17.97 ± 0.02	17.78 ± 0.01	26.04 ± 1.18	56225.84 ± 1.18	56252.69 ± 0.29	$--$	2.000	R
iPTF13agz	-17.74 ± 0.01	19.44 ± 0.01	52.65 ± 1.05	56359.31 ± 0.49	56414.97 ± 1.00	0.0170 ± 0.0003	0.100	R
iPTF13aki	-19.33 ± 0.03	20.28 ± 0.03	13.64 ± 2.91	56387.61 ± 0.93	56403.57 ± 3.27	0.0102 ± 0.0005	5.000	R
iPTF13asr	-18.83 ± 0.04	20.56 ± 0.04	20.27 ± 1.22	56395.26 ± 0.93	56418.66 ± 1.06	$--$	1.000	R
iPTF13cuf	-19.28 ± 0.08	21.00 ± 0.08	$--$	$--$	$--$	$--$	0.300	R
iPTF14bcw	-18.29 ± 0.06	20.52 ± 0.06	$--$	$--$	56821.01 ± 1.71	$--$	1.000	R/r
iPTF14bpa	-20.15 ± 0.06	18.76 ± 0.06	36.05 ± 7.92	56822.87 ± 1.09	56863.31 ± 8.82	0.0056 ± 0.0003	0.700	R/r
iPTF15aym	-18.35 ± 0.02	17.62 ± 0.01	24.51 ± 1.63	57164.31 ± 1.65	57189.64 ± 0.35	0.0242 ± 0.0004	1.000	g
iPTF15bky	-18.44 ± 0.01	17.34 ± 0.01	22.73 ± 0.78	57180.86 ± 0.76	57204.24 ± 0.26	0.0456 ± 0.0014	1.000	g
iPTF15blp	-20.19 ± 0.02	19.74 ± 0.02	20.76 ± 3.06	57180.51 ± 3.39	57205.31 ± 1.38	0.0136 ± 0.0005	0.100	g
iPTF15eqr	-18.33 ± 0.02	19.18 ± 0.02	18.71 ± 1.18	57353.31 ± 0.80	57372.90 ± 0.94	$--$	0.500	R/r
iPTF16fb	-18.47 ± 0.05	19.57 ± 0.05	$--$	$--$	57441.06 ± 3.64	$--$	0.100	g

Note. — The absolute magnitudes are corrected for Milky Way and host-galaxy extinction (Sect. 3.1). The magnitude 1σ uncertainties are taken from the spline fits (Sect. 4.1). The total uncertainty of the rise time is estimated as the uncertainty of the rise time from the MC experiment and the uncertainty of the peak epoch, added in quadrature. The photometric bands are called *R* (Mould R), *r* (SDSS r) and *g* (SDSS g) in the table.

Appendix A: K-corrections for SNe IIn

K-corrections were determined in the g, r, and i bands, while phases refer to the peak of each SN (see Sect. 4.1 and Table 5[5] and are given in the rest frame, hence corrected by a factor $(1+z)$. Owing to the lack of detailed individual spectral sequences, the inferred K-corrections are based on the spectroscopic evolution of the entire sample as a whole, with each spectrum corresponding to a specific phase.

For each object, we take the derived redshift as a reference, shifting all the rest-frame spectra of the sample to that particular z using the IRAF task DOPCOR (called through PYRAF[6]). We then compute synthetic magnitudes on the shifted spectra ($m_{z,t}$) using the IRAF task CALCPHOT included in the software package Space Telescope Science Data Analysis System (STSDAS[7]) and K-corrections ($m_{z,t} - m_{z_0,t}$, where $m_{z_0,t}$ are the synthetic magnitudes computed on the rest-frame spectra). All spectra were previously corrected for the foreground Galactic extinction along the line of sight and, for each filter, we did not consider spectra without the sufficient spectral coverage (i.e., not covering the entire filter bandwidth) after applying the specific redshift correction.

In Fig. A.1 we show the derived K-corrections for each redshift, also including those obtained from other SNe IIn with well-sampled spectroscopic evolutions available in the literature (SNe 1988Z, 1998S, 2010jl, and iPTF16tu[8]; Turatto et al. 1993; Fassia et al. 2001; Fransson et al. 2014; Tartaglia et al. in preparation, respectively). Final values were inferred fitting third-order polynomials to the K-corrections computed at each epoch and 1σ errors were assumed as uncertainties. We find corrections of $\lesssim 0.2$ mag at all phases up to $z \approx 0.1$, while at higher redshifts we start to see a significant scatter in the data points.

Interpolating the derived polynomials at maximum brightness and +50 d, we can estimate the effects of the K-corrections on the photometric properties of our sample (see Fig. A.2). A LSQ fourth-order fit to the r-band K-correction at light-curve peak gives us Eq. A.1, and a LSQ first-order fit to the r-band K-correction errors at light-curve peak gives us Eq. A.2:

$$K_r(z) = 184.16z^4 - 86.69z^3 + 8.96z^2 + 0.95z + 0.01\ \text{mag}, \tag{A.1}$$

$$\text{and } K_r^{\text{Err}}(z) = 0.89z - 0.01\ \text{mag}. \tag{A.2}$$

Eq. A.1 and Eq. A.2 are valid for $z \leq 0.3135$. Note that the errors used for Eq. A.2 are the errors of the fits in Fig. A.1. The data used to make the fits for Eqs. A.1 and A.2 can be found in Table A.1.

At maximum, we see an increase in the K-correction up to $z \approx 0.15$, followed by a flattening around $z \approx 0.2$, while at higher redshifts we see a further increase up to ~ 0.3 mag (although the derived correction at these z is affected by the large scatter in the data points and the lower number of available spectra, owing to the limited spectral coverage). We find a similar evolution in the K-corrections estimated at +50 d, although we do not notice the flattening observed at maximum, while we see a steep decline from ~ 0.18 to ~ 0.9 mag in the $0.15 \lesssim z \lesssim 0.2$ range. In Fig. A.2 (inset) we also show the effect of the derived K-corrections on the slope of light curves in the first 50 d after maximum brightness. We note a maximum deviation of -1.5×10^{-3} mag at $z \approx 0.25$ in the derived slope, suggesting a negligible contribution of the K-correction up to $z \approx 0.3$, while it starts to play an important role in determining magnitudes at peak at $z \gtrsim 0.15$.

---

[5] To allow better sampling of the K-correction at higher redshifts, the SNe PTF10qwu, PTF10acsq and iPTF13cuf (excluded in the main analysis, c.f. Sect. 4.1) are included here, with peak epochs approximated as shown by the 'X' symbols in Fig. 5)

[6] `http://www.stsci.edu/institute/software_hardware/pyraf`

[7] `http://www.stsci.edu/institute/software_hardware/stsdas`

[8] iPTF16tu = PSN J13522411+3941286, Zhang & Wang (2015)

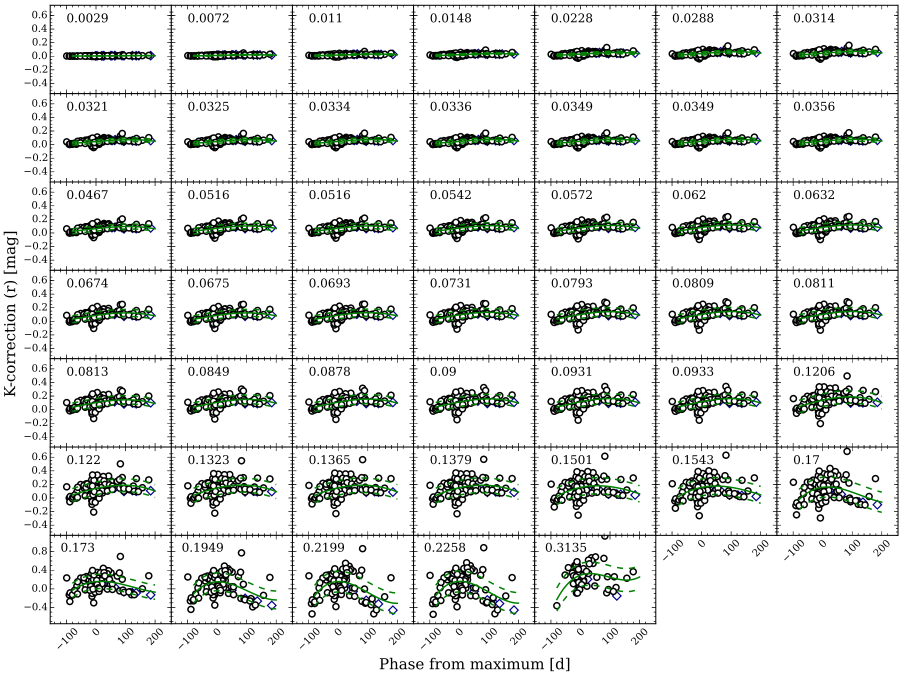

Figure A.1 SN IIn K-corrections for different redshifts in the r-band. Blue points are the corrections computed for well-studied SNe IIn available in the literature (see the text for more details). Green lines are the best-fit models obtained using third-order polynomials, while dashed lines are the 1σ uncertainties of each fit. Phases (rest frame) refer to the estimated light curve peak (Sect. 4.1 and Table 5) of each SN in the sample.

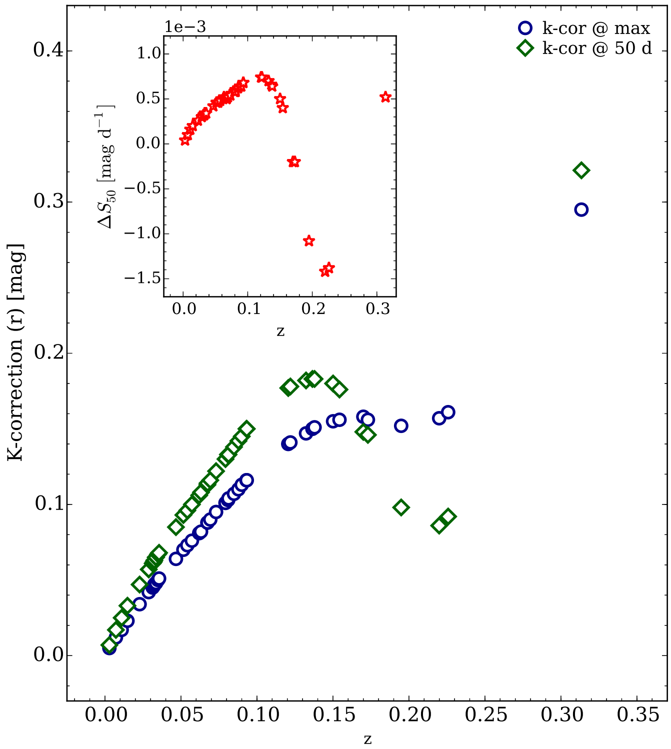

Figure A.2 Effect of the K-correction on photometric properties of our SN IIn sample. The required correction is smaller than $\sim$ 0.2 mag in both peak magnitudes and mag$_{50\,\mathrm{d}}$ at redshifts $\lesssim$ 0.15, although it can be as high as 0.3 mag at $z \gtrsim$ 0.3. The inset shows the effects of the K-correction on the light-curve slopes measured from maximum to +50 d, which is smaller than 1.5×10^{-3} mag for all the redshifts of our sample.

Table A.1. SN IIn K-correction (r-band)

Redshift	$K_{0\ \mathrm{d}}$ (mag)	Error (0 d) (mag)	$K_{50\ \mathrm{d}}$ (mag)	Error (50 d) (mag)
0.0029	0.005	0.003	0.007	0.003
0.0072	0.012	0.007	0.017	0.007
0.0110	0.017	0.010	0.025	0.010
0.0148	0.023	0.013	0.033	0.013
0.0228	0.034	0.019	0.047	0.019
0.0288	0.042	0.024	0.057	0.024
0.0314	0.045	0.026	0.061	0.026
0.0321	0.046	0.026	0.062	0.026
0.0325	0.047	0.027	0.063	0.027
0.0334	0.048	0.027	0.065	0.027
0.0336	0.048	0.028	0.065	0.028
0.0349	0.050	0.029	0.067	0.029
0.0356	0.051	0.029	0.068	0.029
0.0467	0.064	0.037	0.085	0.037
0.0516	0.070	0.041	0.093	0.041
0.0542	0.073	0.043	0.096	0.043
0.0572	0.076	0.045	0.100	0.045
0.0620	0.081	0.049	0.106	0.049
0.0632	0.082	0.049	0.108	0.049
0.0674	0.088	0.052	0.113	0.052
0.0675	0.088	0.052	0.114	0.052
0.0693	0.090	0.053	0.116	0.053
0.0731	0.095	0.055	0.122	0.055
0.0793	0.101	0.060	0.130	0.060
0.0809	0.103	0.061	0.133	0.061
0.0811	0.103	0.061	0.133	0.061
0.0813	0.104	0.061	0.133	0.061
0.0849	0.107	0.064	0.138	0.064
0.0878	0.110	0.066	0.142	0.066
0.0900	0.113	0.068	0.145	0.068
0.0931	0.116	0.070	0.150	0.070
0.0933	0.116	0.070	0.150	0.070
0.1206	0.140	0.093	0.177	0.093
0.1220	0.141	0.094	0.178	0.094
0.1323	0.147	0.103	0.182	0.103
0.1365	0.150	0.106	0.183	0.106
0.1379	0.151	0.107	0.183	0.107
0.1501	0.155	0.119	0.180	0.119
0.1543	0.156	0.124	0.176	0.124
0.1700	0.158	0.148	0.148	0.148
0.1730	0.156	0.154	0.146	0.154
0.1949	0.152	0.192	0.098	0.192
0.2199	0.157	0.223	0.086	0.223
0.2258	0.161	0.227	0.092	0.227
0.3135	0.295	0.248	0.321	0.248

Note. — The K-correction at light-curve peak is called $K_{0\ \mathrm{d}}$, at 50 d (rest frame) after peak it is called $K_{50\ \mathrm{d}}$. The data in this table are also plotted in Fig. A.2.